Numerical Simulations of the Nonlinear Quantum Vacuum in the Heisenberg-Euler Weak-Field Expansion

Andreas Lindner, Baris Ölmez, Hartmut Ruhl

Arnold Sommerfeld Center for Theoretical Physics, Ludwig-Maximilians-Universität München
Theresienstr. 37, D-80333 München, Germany

Abstract

A highly-accurate numerical scheme for solving the nonlinear Heisenberg-Euler equations in up to three spatial dimensions plus time is presented and its properties are discussed. The algorithm is tested in one spatial dimension against a set of already known analytical results of vacuum effects such as birefringence and harmonic generation. Its power to go beyond analytically solvable scenarios is demonstrated in 2D. First parallelization scaling tests are conducted in 3D.

Keywords: Vacuum Polarization, Heisenberg-Euler, Weak-Field Expansion, Simulation, High Harmonics, Birefringence

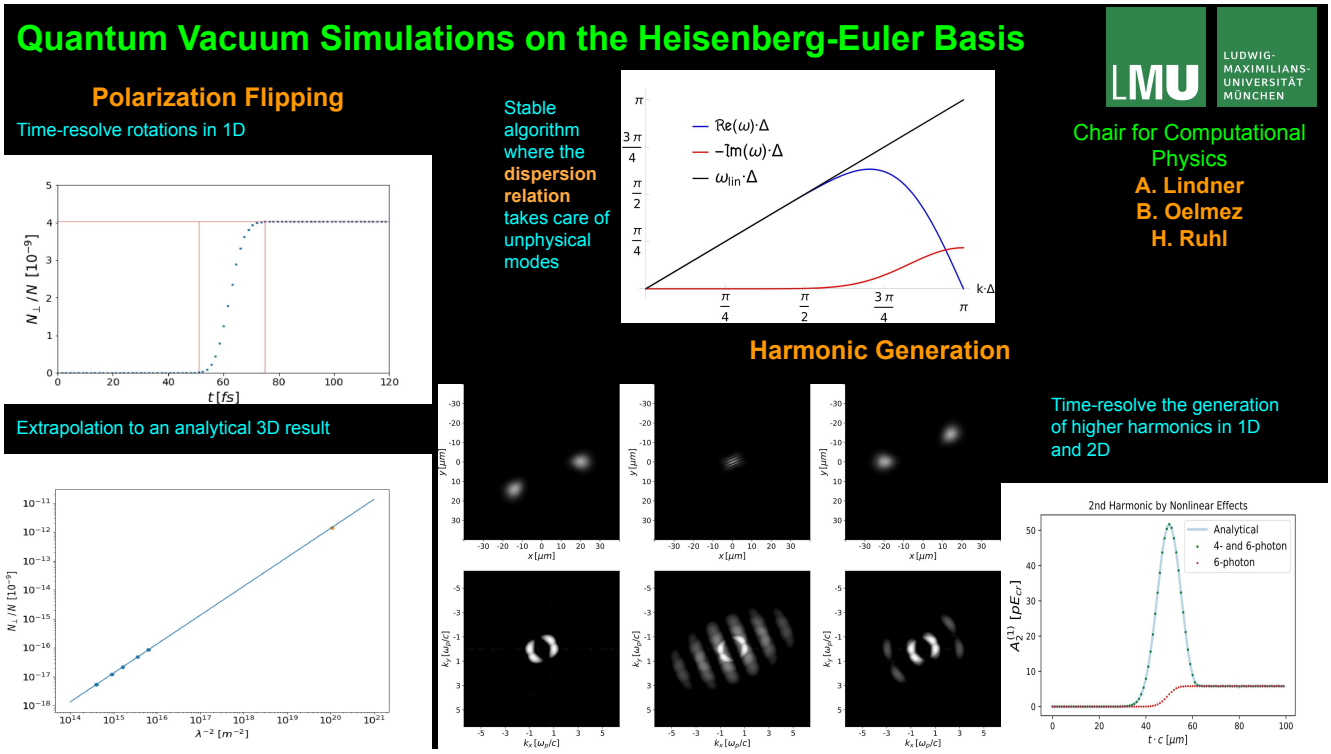

Figure 1: Graphical abstract.

Highlights

- A universal 13th order of accuracy numerical scheme with nonphysical modes filter
- Inclusion of up to 6-photon processes in the Heisenberg-Euler weak-field expansion
- Universality with respect to pulse configurations in contrast to analytical treatments
- Scalability on distributed computing systems
- Versatility in the context of high-precision experiments

Email addresses: and.lindner@physik.uni-muenchen.de (Andreas Lindner), b.oelmez@physik.uni-muenchen.de (Baris Ölmez), hartmut.ruhl@physik.uni-muenchen.de (Hartmut Ruhl)

1. Introduction

Virtual electron-positron pairs in the QED vacuum can mediate effective photon-photon interactions. Taking those into account in the low-energy limit below the Compton scale of the electron, nonlinear terms in the electromagnetic field extend Maxwell's theory. Radiation on the other hand can influence the behavior of the particle-antiparticle dipoles in the vacuum. Therefore, the vacuum of QED with its quantum fluctuations acts as a nonlinear, polarizable medium with quantifiable effects.

The corresponding low-energy effective theory was devised by Heisenberg and Euler [1]. Schwinger incorporated the theory into the larger QED picture [2].

There are numerous non-intuitive effects beside the commonly known Casimir effect and Lamb shift that are due to the quantum nature of the vacuum. Among those are vacuum birefringence [3–5], polarization rotation [6], vacuum diffraction [7–10], dispersion [11], scattering [12], reflection [13], generation of higher harmonics [14, 15], or photon merging [14, 16, 17] and photon splitting [11, 18, 19].

A promising approach to their detection is the investigation of the asymptotic dynamics of *probe* photons after the collision with high-intensity laser pulses. Due to their nonlinear interaction with the power pulses, probe photons scatter in such a way that their dynamics or polarization distinguishes them from the latter. The properties and dynamics of the quantum vacuum, in turn, are hereby encoded into the probe photons.

Nowadays the measurement of nonlinear vacuum effects is either possible or within reach thanks to the tremendous progress in high-intensity laser technology in recent years [20, 21].

Almost all analytical approaches found in the literature to compute nonlinear vacuum effects as, e.g., in [7, 12, 14, 17, 22–37] have shortcomings. As a consequence these attempts are still limited to simple scenarios which most of the time are inappropriate for experimental verification.

The present paper introduces a numerical algorithm for the solution of the weak-field approximation of the Heisenberg-Euler equations [38, 39] [15]. In [38, 39] the numerical scheme outlined in 1D in [15] is extended to full 3D simulations while at the same time the computational load is reduced. The accuracy of the numerical algorithm in [38, 39] relies on the assumptions that the fields vary on scales larger than the Compton scale of the electron and the field strengths involved are below the *critical* field for pair creation in the vacuum. In addition, a viable numerical algorithm is restricted by the computational load it generates especially in the realm of high frequencies. The advantage, however, of a numerical approach is that it can principally solve any interaction scenario for any arrangement of laser pulses.

The numerical predictions of the algorithm are benchmarked with analytical predictions of birefringence as calculated in [27, 28] and higher harmonics as predicted in [17].

1.1. Comparison to other approaches

There are other approaches taken to simulate all-optical QED vacuum effects. The approach in [40] takes the strong electromagnetic fields that are solutions of the linear Maywell equations in the absence of vacuum nonlinearities. These constitute source terms for signal photon emission induced by quantum vacuum nonlinearities. The approach is called the vacuum emission picture [41]. It lacks spatio-temporal resolution but is capable of making predictions for ultra-short emission wavelengths. The high-intensity laser pulses in [40] are propagated by a Maxwell solver detailed in [42]. No distinction of pump and probe laser fields is made and no nonlinearities of the pulses themselves are included in contrast to the scenarios considered throughout the present work. Still, the vacuum emission scheme it is a useful approximation and a very efficient concept. In [43] a generalized Yee scheme of second order accuracy in space and time is devised that follows the ideas of [38]. For comparison, the accuracy order of the numerical scheme in the present paper ranges from second to thirteenth order. It has to be noted that there are some all-optical vacuum nonlinear effects so tiny that high-order, high-precision numerical solvers are required. Our solver is not limited to second order as the work quoted in [43]. The performance of our scheme strongly depends on the accuracy order selected. It can be implemented in the PIC loop just as the implementation of [43]. In the Yee scheme approach interpolations in space and time have to be performed in order to compute nonlinearities and in the generalized method outlined in [43] additional re-interpolations have to be carried out to balance the accuracy in the Yee grid cells. Unlike in the scheme in [43] the dispersion relation outlined in the present paper has an imaginary part that damps nonphysical modes of the underlying grid. There is no amplifying imaginary part as in [43] in the scheme of the present paper. The solver in [43] at present includes only the four photon order of the weak-field expansion of the Heisenberg-Euler interaction and yields a dispersion relation that requires high grid resolutions for given wavelengths. The reason is most likely the amplifying imaginary part. The present work outlines an overall stable algorithm including up to 6-photon interactions with a dispersion relation extremely close to the vacuum dispersion relation up to large wavenumbers at order 13 in the numerical scheme and in addition has an imaginary part that always damps nonphysical modes on the grid.

1.2. Outline

The paper begins with a recap of the weak-field expansion of the Heisenberg-Euler effective theory in section 2. In Maxwell's theory, where there are no light-light interactions, the superposition principle for the set of differential equations holds, i.e., they are linear. In section 3, the nonlinear modifications to Maxwell's equations due to the Heisenberg-Euler theory are shown. In section 4 the simulation algorithm that solves the nonlinear

Maxwell equations in 3+1 dimensions is introduced. In sections 6-9 the power of the Heisenberg-Euler solver is demonstrated by solving various scenarios of nonlinear vacuum phenomena and by successfully benchmarking with analytical results where they exist. In section 6 the phase velocity reduction of a probe pulse propagating through a strong electromagnetic background is successfully compared to analytical predictions for sufficiently large background field strengths. In section 7 the phenomenon of vacuum birefringence is investigated with the help of simulations for probe-pump setups. The theoretical prediction of the polarization flipping probability and its scaling with various parameters is verified and an analytical value of the latter for a special setting computed in [27] is reproduced by extrapolations to the x-ray regime. In section 8 the capability of the simulation algorithm to predict higher harmonics in the vacuum is demonstrated. It is shown that for specific settings analytical results from [17] are accurately reproduced in the simulations presented in this work. Examples of harmonic generation in 2D simulations are presented in section 9. The latter are hard, if not impossible, to obtain by analytical means. The 2D results are used for comparison with the previous 1D simulations. Higher-dimensional simulations enable the investigation of complicated scenarios that cannot be solved analytically in the future. The paper is concluded with a summary and an outlook to future research employing the Heisenberg-Euler solver in section 10.

2. Heisenberg-Euler Lagrangian

Following the derivation by Schwinger [2] the Heisenberg-Euler Lagrangian reads

$$\mathcal{L}_{HE} = -\frac{c^5 m^4}{8\hbar^3\pi^2}\int_0^\infty \frac{e^{-s}}{s^3}\left(\frac{s^2}{3}\left(a^2-b^2\right) - 1 + abs^2\cot(as)\coth(bs)\right) ds \ , \tag{1}$$

where

$$a = \sqrt{\sqrt{\mathcal{F}^2+\mathcal{G}^2}+\mathcal{F}} \ , \quad b = \sqrt{\sqrt{\mathcal{F}^2+\mathcal{G}^2}-\mathcal{F}} \ , \tag{2}$$

$$\mathcal{F} = -\frac{c^2 F^{\mu\nu}F_{\mu\nu}}{4E_{cr}^2} \ , \quad \mathcal{G} = -\frac{c^2 F^{\mu\nu}F^*_{\mu\nu}}{4E_{cr}^2} \ , \tag{3}$$

$$E_{cr} = \frac{m^2c^3}{e\hbar} = 1.323\times 10^{18}\frac{\mathrm{V}}{\mathrm{m}} \ , \tag{4}$$

and m is the mass of the electron. The quantities F and F^* denote the electromagnetic tensor and its dual and E_{cr} is the critical field strength, which is an important scale for the magnitude of the vacuum nonlinearities. The Lagrangian for the quantum vacuum is given by

$$\mathcal{L} = \frac{c^5m^4}{\hbar^3}\mathcal{L}_{MW} + \mathcal{L}_{HE} = \frac{c^5m^4}{\hbar^3}\mathcal{F} + \mathcal{L}_{HE} \quad \text{and} \quad \mathcal{L}_{MW} = \frac{c^5m^4}{\hbar^3}\mathcal{F} \ , \tag{5}$$

where $\mathcal{L}_{MW}$ is the normalized free Maxwell Lagrangian. To derive $\mathcal{L}_{HE}$ it has been assumed that the constant background approximation is valid [44, 45] due to the fact that the variations of the field strengths are small on the scale of the Compton wavelength [46]

$$\lambda_C = \frac{\hbar}{mc} = 2.426\times 10^{-12}\mathrm{m} \ . \tag{6}$$

Since the integral in (1) is hard to evaluate explicitly the so-called weak-field expansion is performed to simplify the integral expressions. The explicit form of the Heisenberg-Euler Lagrangian in the weak-field expansion up to the forth order in a and b is given by

$$\mathcal{L}_{HE} \approx \frac{c^5m^4}{360\hbar^3\pi^2}\left(4\mathcal{F}^2+7\mathcal{G}^2\right) \tag{7a}$$

$$+\frac{c^5m^4}{630\hbar^3\pi^2}\left(8\mathcal{F}^3+13\mathcal{F}\mathcal{G}^2\right) \tag{7b}$$

$$+\frac{c^5m^4}{945\hbar^3\pi^2}\left(48\mathcal{F}^4+88\mathcal{F}^2\mathcal{G}^2+19\mathcal{G}^4\right) \ . \tag{7c}$$

It should be noted that the Heisenberg-Euler Lagrangian solely depends on electromagnetic invariants and subsequently (7a) is of the order $\mathcal{O}((E/E_{cr})^4)$. The effective interaction $\mathcal{L}_{HE}$ can be graphically represented by a double-lined loop as in figure 2 to the left. As a consequence, (7a) represents the four-photon contributions, (7b) the six-photon contributions, and (7c) the eight-photon contribution to the closed loop as illustrated in figure 2. Since the electric field strength is normalized to the critical field strength with $c|F_{\mu\nu}| \ll E_{cr}$, higher order terms can be neglected in the low intensity regime.

It has to be mentioned that pair production is exponentially suppressed in the complete Heisenberg-Euler Lagrangian for $c|F_{\mu\nu}| \ll E_{cr}$. Therefore, the properties of the nonlinear vacuum can be described exclusively by radiation fields.

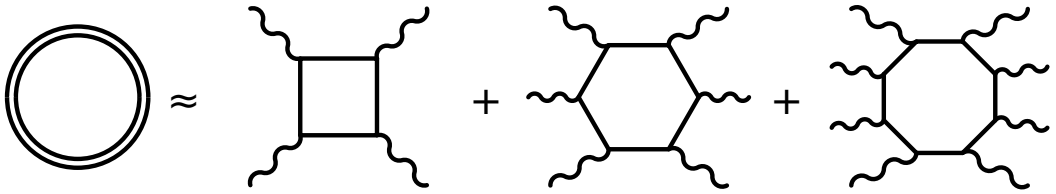

Figure 2: Depiction of the weak-field expansion of the Heisenberg-Euler Lagrangian. The double-lined loop to the left represents $\mathcal{L}_{HE}$ while the diagrams to the right are the 4-, 6-, and 8-photon contributions due to the weak-field expansion of $\mathcal{L}_{HE}$ corresponding to (7a),(7b), and (7c).

3. Modified Maxwell Equations

To obtain the nonlinear modifications to the linear Maxwell equations an explicit rescaling of the Maxwell Lagrangian to the critical field strengths is performed

$$\mathcal{L}_{MW} = -\frac{1}{4\mu_0} F^{\mu\nu} F_{\mu\nu} \xrightarrow{E \to \frac{E}{E_{cr}}} \mathcal{L}_{MW} = -\frac{1}{4\mu} F^{\mu\nu} F_{\mu\nu} \tag{8}$$

with the vacuum permeability

$$\mu_0 = 1.257 \times 10^{-6} \frac{\mathrm{kg\,m}}{\mathrm{s^2 A^2}} \tag{9}$$

and the definition

$$\mu = \frac{\hbar^2 e^2}{m^4 c^6}\, \mu_0 = 7.176 \times 10^{-43} \frac{\mathrm{s^4}}{\mathrm{kg\,m}} \ . \tag{10}$$

From the Lagrangian of the quantum vacuum (5) the equations of motion are obtained with the help of the Euler-Lagrange equations

$$\partial_t \left(\vec{E} + \mu \frac{\partial \mathcal{L}_{HE}}{\partial \vec{E}} \right) = \nabla \times \left(\vec{B} - \mu \frac{\partial \mathcal{L}_{HE}}{\partial \vec{B}} \right) \ . \tag{11}$$

The classical Maxwell equations [47]

$$\partial_t \vec{B} = -\nabla \times \vec{E} \ , \tag{12a}$$

$$\partial_t \left(\vec{E} + \vec{P} \right) = \nabla \times \left(\vec{B} - \vec{M} \right) \tag{12b}$$

are compared to (11) in such a way that photon-photon interactions are included, which implies the appearance of macroscopic nonlinear polarization and magnetization terms given by

$$\vec{P} = \mu \frac{\partial \mathcal{L}_{HE}}{\partial \vec{E}} \quad \text{and} \quad \vec{M} = \mu \frac{\partial \mathcal{L}_{HE}}{\partial \vec{B}}. \tag{13}$$

4. Numerical Method and Dispersion Effects

The two modified Maxwell equations (12) are merged and a single partial differential equation that describes the whole dynamics of the system is formulated. The curl of $(\vec{B} - \vec{M})$ can be written as

$$\begin{aligned} \nabla \times (\vec{B} - \vec{M}) = &\underbrace{\begin{pmatrix} 0 & 0 & 0 \\ 0 & 0 & -1 \\ 0 & 1 & 0 \end{pmatrix}}_{\mathbf{Q}_x} \partial_x (\vec{B} - \vec{M}) + \underbrace{\begin{pmatrix} 0 & 0 & 1 \\ 0 & 0 & 0 \\ -1 & 0 & 0 \end{pmatrix}}_{\mathbf{Q}_y} \partial_y (\vec{B} - \vec{M}) \\ &+ \underbrace{\begin{pmatrix} 0 & -1 & 0 \\ 1 & 0 & 0 \\ 0 & 0 & 0 \end{pmatrix}}_{\mathbf{Q}_z} \partial_z (\vec{B} - \vec{M}) = \sum_{j \in \{x;y;z\}} \mathbf{Q}_j \partial_j (\vec{B} - \vec{M}) \,, \end{aligned} \tag{14}$$

with the help of (13), (14), and the vector

$$\vec{f} = \left(\vec{E}, \vec{B} \right)^{\mathrm{T}} \ , \tag{15}$$

where $\vec{E}$ and $\vec{B}$ are the electric and magnetic fields, (12) results in

$$(\mathbf{1}_6 + \mathbf{A})\,\partial_t \vec{f} = \sum_{j\in\{x;y;z\}} \mathbf{Z}_j \partial_j \vec{f}\,. \tag{16}$$

The matrices $\mathbf{A}$ and $\mathbf{Z}_j$ are given by

$$\mathbf{A} = \begin{pmatrix} \mathbf{J}_{\vec{P}}\left(\vec{E}\right) & \mathbf{J}_{\vec{P}}\left(\vec{B}\right) \\ \mathbf{0}_3 & \mathbf{0}_3 \end{pmatrix}\,,\ \mathbf{Z}_j = \begin{pmatrix} -\mathbf{Q}_j\mathbf{J}_{\vec{M}}\left(\vec{E}\right) & \mathbf{Q}_j - \mathbf{Q}_j\mathbf{J}_{\vec{M}}\left(\vec{B}\right) \\ -\mathbf{Q}_j & \mathbf{0}_3 \end{pmatrix}, \tag{17}$$

where

$$\mathbf{J}_{\vec{P}}(\vec{E}) = \frac{\partial \vec{P}}{\partial \vec{E}}\,,\quad \mathbf{J}_{\vec{P}}(\vec{B}) = \frac{\partial \vec{P}}{\partial \vec{B}}\,,\quad \mathbf{J}_{\vec{M}}(\vec{E}) = \frac{\partial \vec{M}}{\partial \vec{E}}\,,\quad \mathbf{J}_{\vec{M}}(\vec{B}) = \frac{\partial \vec{M}}{\partial \vec{B}}\,. \tag{18}$$

Equations (16) contain the full dynamics of the electromagnetic fields in weak-field approximation of the Heisenberg-Euler model. For simplicity, first the linear vacuum is considered by setting $\vec{P} = \vec{M} = 0$ leading to

$$\partial_t \vec{f} = \sum_{j\in\{x;y;z\}} \mathbf{Z}_j^{\mathrm{lin}} \partial_j \vec{f}\,,\quad \mathbf{Z}_j^{\mathrm{lin}} = \begin{pmatrix} 0 & \mathbf{Q}_j \\ -\mathbf{Q}_j & 0 \end{pmatrix}. \tag{19}$$

For later purposes $\mathbf{Z}_j^{\mathrm{lin}}$ is diagonalized using the rotation matrices

$$\begin{aligned}
\mathbf{R}_x &= \frac{1}{\sqrt{2}}\begin{pmatrix} \sqrt{2} & 0 & 0 & 0 & 0 & 0 \\ 0 & 1 & 0 & 0 & 0 & -1 \\ 0 & 0 & 1 & 0 & 1 & 0 \\ 0 & 0 & 0 & \sqrt{2} & 0 & 0 \\ 0 & 1 & 0 & 0 & 0 & 1 \\ 0 & 0 & 1 & 0 & -1 & 0 \end{pmatrix},\ \mathbf{R}_y = \frac{1}{\sqrt{2}}\begin{pmatrix} 0 & \sqrt{2} & 0 & 0 & 0 & 0 \\ -1 & 0 & 0 & 0 & 0 & -1 \\ 0 & 0 & -1 & 1 & 0 & 0 \\ 0 & 0 & 0 & 0 & \sqrt{2} & 0 \\ -1 & 0 & 0 & 0 & 0 & 1 \\ 0 & 0 & -1 & -1 & 0 & 0 \end{pmatrix}, \\
\mathbf{R}_z &= \frac{1}{\sqrt{2}}\begin{pmatrix} 0 & 0 & \sqrt{2} & 0 & 0 & 0 \\ 1 & 0 & 0 & 0 & -1 & 0 \\ 0 & 1 & 0 & 1 & 0 & 0 \\ 0 & 0 & 0 & 0 & 0 & \sqrt{2} \\ 1 & 0 & 0 & 0 & 1 & 0 \\ 0 & 1 & 0 & -1 & 0 & 0 \end{pmatrix},
\end{aligned} \tag{20}$$

so that for $\mathbf{Z}_j^{\mathrm{lin}}$ the expressions

$$\mathbf{Z}_j^{\mathrm{lin}} = \mathbf{R}_j^{\mathrm{T}} \begin{pmatrix} 0 & 0 & 0 & 0 & 0 & 0 \\ 0 & 1 & 0 & 0 & 0 & 0 \\ 0 & 0 & 1 & 0 & 0 & 0 \\ 0 & 0 & 0 & 0 & 0 & 0 \\ 0 & 0 & 0 & 0 & -1 & 0 \\ 0 & 0 & 0 & 0 & 0 & -1 \end{pmatrix} \mathbf{R}_j = \mathbf{R}_j^{\mathrm{T}} \mathrm{diag}(0,1,1,0,-1,-1)\mathbf{R}_j \tag{21}$$

are obtained. Now (19) becomes

$$\partial_t \mathbf{R}_j \vec{f}(x,y,z) = \mathrm{diag}(0,1,1,0,-1,-1)\,\partial_j \mathbf{R}_j \vec{f}(x,y,z)\ , \tag{22}$$

where

$$\mathbf{R}_x\vec{f} = \frac{1}{\sqrt{2}}\begin{pmatrix} \sqrt{2}E_x \\ E_y - B_z \\ E_x + B_y \\ \sqrt{2}B_x \\ E_y + B_z \\ E_z - B_y \end{pmatrix}\quad,\quad \mathbf{R}_y\vec{f} = \frac{1}{\sqrt{2}}\begin{pmatrix} \sqrt{2}E_y \\ -B_z - E_x \\ B_x - E_z \\ \sqrt{2}B_y \\ B_z - E_x \\ -B_x - E_z \end{pmatrix}\quad,\quad \mathbf{R}_z\vec{f} = \frac{1}{\sqrt{2}}\begin{pmatrix} \sqrt{2}E_z \\ -B_y + E_x \\ B_x + E_y \\ \sqrt{2}B_z \\ B_y + E_x \\ -B_x + E_y \end{pmatrix}. \tag{23}$$

Equations (22) and (23) imply backward propagation in x-direction of the field components $(E_y - B_z)$ and $(E_x + B_y)$, forward propagation of the field components $(E_y + B_z)$ and $(E_z - B_y)$, and non-propagation of the first and forth component. Analogously for the other directions.

For demonstration purposes only the x-direction is considered in the following. In order to transform the partial differential equation into an ordinary one, finite difference approximations are introduced. The spatial derivative ∂_x is replaced by finite differences

$$\partial_t \left(\mathbf{R}_x \vec{f}\right)(x,y,z) = \mathcal{D}_x \left(\mathbf{R}_x \vec{f}\right)(x,y,z)\,, \tag{24}$$

where

$$\mathcal{D}_x \left(\mathbf{R}_x \vec{f}\right)(x,y,z) = \sum_\nu \frac{1}{\Delta_x} S_\nu \left(\mathbf{R}_x \vec{f}\right)(x+\nu\Delta_x,y,z)\ . \tag{25}$$

The S_ν are stencil matrices and Δ_x is the spatial resolution. Now the stencil matrices S_ν are derived with the help of a Taylor expansion of the function $g(x+\nu\Delta_x)$ around $\nu\Delta_x = 0$. The Taylor expansion of g to 6th order accuracy is given by

$$\begin{aligned} g(x+\nu\Delta_x) = g(x) + (k\cdot\Delta_x)\,g(x) + \frac{1}{2}(\nu\cdot\Delta_x)^2 g''(x) + \frac{1}{6}(\nu\cdot\Delta_x)^3 g'''(x) + \frac{1}{24}(\nu\cdot\Delta_x)^4 g^{(4)}(x) \\ + \frac{1}{120}(\nu\cdot\Delta_x)^5 g^{(5)}(x) + \frac{1}{720}(\nu\cdot\Delta_x)^6 g^{(6)}(x) + \mathcal{O}\left((\nu\cdot\Delta_x)^7\right)\ . \end{aligned} \tag{26}$$

For the finite difference approximation of the first derivative the forward and backward finite differences are used. For the values $\nu \in \{-3,...,3\}$ the expansion in matrix form reads

$$\begin{pmatrix} g(x-3\Delta_x) \\ g(x-2\Delta_x) \\ g(x-\Delta_x) \\ g(x) \\ g(x+\Delta_x) \\ g(x+2\Delta_x) \\ g(x+3\Delta_x) \end{pmatrix} = \begin{pmatrix} 1 & -3 & 9/2 & -9/2 & 27/8 & -81/40 & 81/80 \\ 1 & -2 & 2 & -4/3 & 2/3 & -4/15 & 4/45 \\ 1 & -1 & 1/2 & -1/6 & 1/24 & -1/120 & 1/720 \\ 1 & 0 & 0 & 0 & 0 & 0 & 0 \\ 1 & 1 & 1/2 & 1/6 & 1/24 & 1/120 & 1/720 \\ 1 & 2 & 2 & 4/3 & 2/3 & 4/15 & 4/45 \\ 1 & 3 & 9/2 & 9/2 & 27/8 & 81/40 & 81/80 \end{pmatrix} \cdot \begin{pmatrix} g(x) \\ \Delta_x g'(x) \\ \Delta_x^2 g''(x) \\ \Delta_x^3 g'''(x) \\ \Delta_x^4 g^{(4)}(x) \\ \Delta_x^5 g^{(5)}(x) \\ \Delta_x^6 g^{(6)} x) \end{pmatrix}\ . \tag{27}$$

To illustrate how the finite difference approximation of the first derivative is calculated $\nu \in \{0,1\}$ is considered, for simplicity. It is obtained

$$\begin{pmatrix} g(x) \\ g(x+\Delta_x) \end{pmatrix} = \begin{pmatrix} 1 & 0 \\ 1 & 1 \end{pmatrix} \cdot \begin{pmatrix} g(x) \\ \Delta_x g'(x) \end{pmatrix}\ , \tag{28}$$

which leads to the first derivative of g given by

$$g'(x) \approx g'_{\nu\in\{0,1\}} = \frac{g(x+\Delta_x)-g(x)}{\Delta_x}\,. \tag{29}$$

The derivative $g'_{\nu\in\{0,1\}}$ in (29) is called first order forward discrete derivative. In the same way the first order backward discrete derivative $g'_{\nu\in\{-1,0\}}$ is obtained with the help of

$$\begin{pmatrix} g(x-\Delta_x) \\ g(x) \end{pmatrix} = \begin{pmatrix} 1 & -1 \\ 1 & 0 \end{pmatrix} \cdot \begin{pmatrix} g(x) \\ \Delta_x g'(x) \end{pmatrix}\ , \tag{30}$$

where

$$g'_{\nu\in\{-1,0\}} = \frac{g(x)-g(x-\Delta_x)}{\Delta_x}\,. \tag{31}$$

In order to obtain specific dispersion properties and numerical stability of the discretized equations (22) it is necessary to introduce forward and backward finite differences for $\mathcal{D}_x$ as is discussed below. Recall from (25) that

$$\partial_x \vec{f}(x,y,z) = \mathbf{R}_x^{\mathrm{T}} \partial_x \mathbf{R}_x \vec{f}(x,y,z) \approx \mathbf{R}_x^{\mathrm{T}} \sum_\nu \frac{1}{\Delta_x} S_\nu \left(\mathbf{R}_x \vec{f}\right)(x+\nu\Delta_x,y,z) = \mathbf{R}_x^{\mathrm{T}} \mathcal{D}_x \left(\mathbf{R}_x \vec{f}\right)(x,y,z)\,. \tag{32}$$

The first three elements of the field vector $\mathbf{R}_x \vec{f}$ represent forward propagating electromagnetic modes, while the last three components of the latter represent backward propagating ones when disregarding non-propagating modes, as discussed above for equations (22),(23).

To investigate dispersion effects in the finite difference approximation an easy example is shown in the following. For the values $\nu \in \{-1, 0, 1\}$ the expansion in matrix form is given by

$$\begin{pmatrix} g(x-\Delta_x) \\ g(x) \\ g(x+\Delta_x) \end{pmatrix} = \begin{pmatrix} 1 & -1 & 1/2 \\ 1 & 0 & 0 \\ 1 & 1 & 1/2 \end{pmatrix} \cdot \begin{pmatrix} g(x) \\ \Delta_x g'(x) \\ \Delta_x^2 g''(x) \end{pmatrix} . \tag{33}$$

It has to be noted that equation (33) does not restrict ourselves to one specific kind of finite difference method. To obtain an expression for the first derivative the matrix in (33) has to be inverted. This leads to

$$\begin{pmatrix} g(x) \\ \Delta_x g'(x) \\ \Delta_x^2 g''(x) \end{pmatrix} = \begin{pmatrix} 0 & 1 & 0 \\ -1/2 & 0 & 1/2 \\ 1 & -2 & 1 \end{pmatrix} \cdot \begin{pmatrix} g(x-\Delta_x) \\ g(x) \\ g(x+\Delta_x) \end{pmatrix} . \tag{34}$$

Let us assume that $g(x)$ is one of the two polarizations of an electromagnetic mode that propagates in positive $(+)$ or negative $(-)$ x-direction in 1D. Then the corresponding equation of motion reads

$$(\partial_t \pm c\,\partial_x)\, g_\pm(x;t) = 0\,. \tag{35}$$

Making use of (34) equation (35) becomes for symmetric forward and backward differentiation

$$\partial_t g_\pm(x;t) \pm \frac{c}{2\Delta_x} \left(g_\pm(x+\Delta_x;t) - g_\pm(x-\Delta_x;t)\right) = 0\,, \tag{36}$$

where the spatial derivative of g is accurate up to second order in Δ_x. Equation (36) can be solved analytically by a plane wave ansatz

$$g_\pm(x;t) = e^{-i\omega t + i k_\pm x}\,, \tag{37}$$

where $k_+ > 0$ and $k_- < 0$ to obtain

$$-\left(\omega_R + i\omega_I\right) \pm \frac{c}{\Delta_x} \sin\left(k_\pm \Delta_x\right) = 0\,, \tag{38}$$

$$\omega = \pm \frac{c}{\Delta_x} \sin(k_\pm \Delta_x)\,. \tag{39}$$

However, the derivative in (35) can also be approximated for a forward propagating mode g_+ by a first order forward finite difference. In this case (36) can be written as

$$\partial_t g_+(x;t) + \frac{c}{\Delta_x} \left(g_+(x+\Delta_x;t) - g_+(x;t)\right) = 0\,, \tag{40}$$

where the solution of (40) with $\omega \in \mathbb{C}$ reads

$$-\omega + \frac{c}{\Delta_x} \left(\sin(k_+\Delta_x) + i - i\cos(k_+\Delta_x)\right) = 0\,, \tag{41}$$

$$\mathfrak{Re}(\omega) = \frac{c}{\Delta_x} \sin(k_+\Delta_x)\,, \tag{42}$$

$$\mathfrak{Im}(\omega) = \frac{c}{\Delta_x} \left(1 - \cos(k_+\Delta_x)\right)\,. \tag{43}$$

Next, the derivative in (35) for the backward propagating part can be approximated by a first order backward finite difference. In this case (36) can be approximated for the backward propagating case as

$$\partial_t g_-(x;t) - \frac{c}{\Delta_x} \left(g_-(x;t) - g_-(x-\Delta_x;t)\right) = 0 \tag{44}$$

with the solution

$$-\omega - \frac{c}{\Delta_x}\left(\sin(k_-\Delta_x) - i + i\cos(k_-\Delta_x)\right) = 0\,, \tag{45}$$

$$\mathfrak{Re}(\omega) = -\frac{c}{\Delta_x}\sin(k_-\Delta_x)\,, \tag{46}$$

$$\mathfrak{Im}(\omega) = \frac{c}{\Delta_x}\left(1 - \cos(k_-\Delta_x)\right)\,. \tag{47}$$

The dispersion relations connect a simulated wave with a specified wavelength to its phase velocity on the lattice. While in the symmetric case there is no imaginary part of ω, it does show up for antisymmetric differentiation. The derived dispersion relations are shown on the left and in the middle of figure 3 for the vacuum speed of light c set to 1. The Nyquist frequency $f_{Ny} = \Delta^{-1}/2$, corresponding to $k \cdot \Delta = \pi$, marks the point where $\mathfrak{Re}(\omega) = 0$ in all cases.

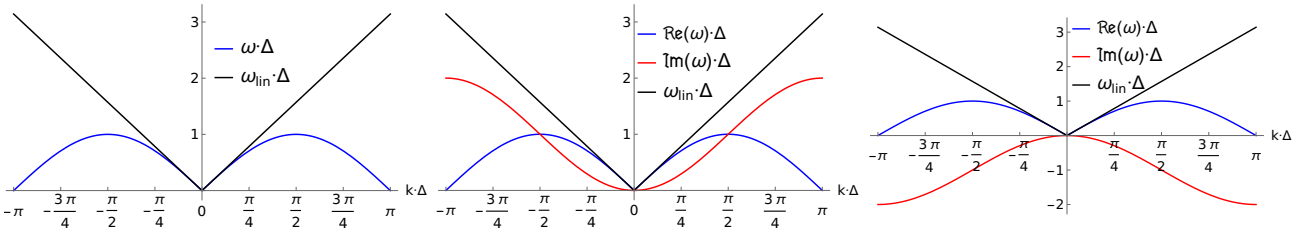

Figure 3: Dispersion relations obtained with low order finite differences for a simple plane wave. Left: for a second order symmetric forward and backward finite difference scheme. Middle: for a first order forward finite difference for the forward propagating part and a first order backward finite difference for the backward propagating part. Right: for a first order forward finite difference for the backward propagating part and a first order backward finite difference for the forward propagating part. The linear vacuum is given as the black line for reference. Note that all the stencils result in a symmetric dispersion relation. The phase velocity is the same for both directions.

The imaginary part amplifies the wave and thus makes this scheme unstable. By differentiating biased against the propagation direction however, the imaginary part switches signs and has a damping effect. The calculations are straightforward and the result is shown on the right of figure 3. This behavior can be tuned with higher order schemes in order to get a more vacuum-like real part and to defer the imaginary part such that it becomes relevant only for short wavelengths and damps them. As the real part of ω eventually decreases in any scheme, the damping of those waves serves as anti-aliasing effect. This is shown below.

Furthermore, when the differentiation is chosen to be balanced, then $S_\nu = 0$ as in (36). This implies that the derivative of g is independent of g itself which causes numerical instabilities in the form of mesh drifts [48]. Biasing the derivatives combats these instabilities but in turn causes a non-isotropic simulation space. The propagation speed of waves decreases in the direction, where the stencil is heavier weighted. The effects on the phase velocity by the non-isotropic space are also eased by applying the backward biased differentiation to the forward propagating components and vice versa and by going to the eigenspace of Z, which is the purpose of the rotations.

Now, the unbalanced coefficients for the first order discrete derivative in fourth order accuracy in Δ_x, $g'_{\nu\in\{-3,1\}}$ and $g'_{\nu\in\{-1,3\}}$ in the above notation, are derived with the help of (27). This results in

$$\begin{aligned}
\Delta_x g'_{\nu\in\{-3,1\}} &= \begin{pmatrix} -1/12 & 1/2 & -3/2 & 5/6 & 1/4 \end{pmatrix} \begin{pmatrix} g(x-3\Delta_x) \\ g(x-2\Delta_x) \\ g(x-\Delta_x) \\ g(x) \\ g(x+\Delta_x) \end{pmatrix}\,, \\
\Delta_x g'_{\nu\in\{-1,3\}} &= \begin{pmatrix} -1/4 & -5/6 & 3/2 & -1/2 & 1/12 \end{pmatrix} \begin{pmatrix} g(x-\Delta_x) \\ g(x) \\ g(x+\Delta_x) \\ g(x+2\Delta_x) \\ g(x+3\Delta_x) \end{pmatrix}\,.
\end{aligned} \tag{48}$$

To make the connection to (24) g is replaced by the components of $\mathbf{R}_x\vec{f}$. As explained above, $\mathbf{R}_x\vec{f}$ has components propagating in different directions that are differentiated with biases in the respective opposite direction. This means that the first three components of $\mathbf{R}_x\vec{f}$ are differentiated as g in the first line of (48) and the last three components of $\mathbf{R}_x\vec{f}$ are differentiated as g in the second line of (48). Following these instructions for equation (25) yields

$$\mathcal{D}_x\left(\mathbf{R}_x\vec{f}\right)(x,y,z)=\sum_{\nu=-3}^{3}\frac{1}{\Delta_x}S_\nu\left(\mathbf{R}_x\vec{f}\right)(x+\nu\Delta_x,y,z) \tag{49}$$

with the stencils given by

$$\begin{aligned}
S_{+3}&=\frac{1}{\Delta_x}\mathrm{diag}(1/12,1/12,1/12,0,0,0)\,, & S_{-3}&=\frac{1}{\Delta_x}\mathrm{diag}(0,0,0,-1/12,-1/12,-1/12)\,,\\
S_{+2}&=\frac{1}{\Delta_x}\mathrm{diag}(-1/2,-1/2,-1/2,0,0,0)\,, & S_{-2}&=\frac{1}{\Delta_x}\mathrm{diag}(0,0,0,1/2,1/2,1/2)\,,\\
S_{+1}&=\frac{1}{\Delta_x}\mathrm{diag}(3/2,3/2,3/2,1/4,1/4,1/4)\,, & S_{-1}&=\frac{1}{\Delta_x}\mathrm{diag}(-1/4,-1/4,-1/4,-3/2,-3/2,-3/2)\,,\\
S_0&=\frac{1}{\Delta_x}\mathrm{diag}(-5/6,-5/6,-5/6,5/6,5/6,5/6)\,.
\end{aligned} \tag{50}$$

The solver has implementations of schemes up to order thirteen. In the present work the currently maximum available accuracy is used. By going seven steps of Δ_x forward and six steps backward in the forward biased differentiation and vice versa in the backward biased case, the unbalance is kept small. The low-bias approximations to order thirteen are given by

$$\begin{aligned}
\Delta_x g'_{\nu\in\{-7,6\}} &= \big(\,-1/12012\quad 1/792\quad -1/110\quad 1/24\quad -5/36\quad 3/8\quad -1\quad 1/7\quad 3/4\\
&\qquad -5/24\quad 1/18\quad -1/88\quad 1/660\quad -1/10296\big)\;\cdot\;\begin{pmatrix} g(x-7\Delta_x)\\ \vdots\\ g(x+6\Delta_x)\end{pmatrix}\,,\\
\Delta_x g'_{\nu\in\{-6,7\}} &= \big(1/10296\quad -1/660\quad 1/88\quad -1/18\quad 5/24\quad -3/4\quad -1/7\quad 1\quad -3/8\quad 5/36\\
&\qquad -1/24\quad 1/110\quad -1/792\quad 1/12012\big)\;\cdot\;\begin{pmatrix} g(x-6\Delta_x)\\ \vdots\\ g(x+7\Delta_x)\end{pmatrix}\,.
\end{aligned} \tag{51}$$

For the nonlinear vacuum the system of ODEs is obtained from (16), (32) to be

$$\partial_t\vec{f}=(\mathbf{1}_6+\mathbf{A})^{-1}\sum_{j\in\{x,y,z\}}\mathbf{Z}_j\mathbf{R}_j^{\mathrm{T}}\mathcal{D}_j\mathbf{R}_j\vec{f}\,. \tag{52}$$

The inversion of $(\mathbf{1}_6+\mathbf{A})$ is an expensive operation. An approximation in terms of a truncated geometric series is not satisfying as also larger nonlinear corrections ought to be taken into account. The problem of inverting the matrix can be reduced from a 6×6 dimensional problem to a 3×3 dimensional one by making use of the block form in (17) such that [39]

$$(\mathbf{1}_6+\mathbf{A})^{-1}=\begin{pmatrix}\mathbf{1}_3+\mathbf{J}_{\vec{P}}\left(\vec{E}\right) & \mathbf{J}_{\vec{P}}\left(\vec{B}\right)\\ \mathbf{0}_3 & \mathbf{1}_3\end{pmatrix}\;=\;\begin{pmatrix}\mathbf{C}^{-1} & -\mathbf{C}^{-1}\mathbf{J}_{\vec{P}}\left(\vec{B}\right)\\ \mathbf{0}_3 & \mathbf{1}_3\end{pmatrix}\,, \tag{53}$$

with

$$\mathbf{C}=\mathbf{1}_3+\mathbf{J}_{\vec{P}}\left(\vec{E}\right)\;. \tag{54}$$

This 3×3 matrix can be inverted explicitly. A numerical solver to be discussed below in subsection 5.1 is responsible for the time integration of the ODE.

For a single plane wave the Heisenberg-Euler Lagrangian reduces to the Maxwell Lagrangian as $\mathcal{F}=\mathcal{G}=0$. The vacuum is the linear one. Inserting a forward propagating plane wave

$$\vec{E}(\vec{x};t)=\vec{A}\,e^{-i(\omega t-\vec{k}\cdot\vec{x})}$$

into the propagation equation (52) yields the constraint

$$\det\left(i\omega\mathbf{1}_6+\sum_{j\in\{x,y,z\}}\mathbf{Z}^{\mathrm{lin}}\,\mathbf{R}_j^{\mathrm{T}}\sum_\nu S_\nu e^{i\nu k_j\Delta_j}\mathbf{R}_j\right)=0\,. \tag{55}$$

Solving for the real and imaginary parts of ω gives

$$\mathfrak{Re}(\omega) = \left\| \mathfrak{Im}\left(\sum_{j\in\{x,y,z\}} \sum_{\nu} S_\nu e^{i\nu k_j \Delta_j} \mathbf{Z}^{\text{lin}} \right) \right\| \quad \text{and} \quad -\mathfrak{Im}(\omega) = \left\| \mathfrak{Re}\left(\sum_{j\in\{x,y,z\}} \sum_{\nu} S_\nu e^{i\nu k_j \Delta_j} \mathbf{Z}^{\text{lin}} \right) \right\|, \tag{56}$$

where $\|\bullet\|$ denotes the matrix norm. The rotation matrices cancel in the final analytical expressions. The results are visualized in figure 4 for propagation along one axis with the fourth order stencils (50) and the order 13 stencils obtained from (51) which are the ones used for the simulations in this work. The spacing between the lattice points Δ, the resolution of the lattice, is the decisive parameter to tune the dispersive effects for any given wavelength. It is given by the ratio of physical length and lattice points.

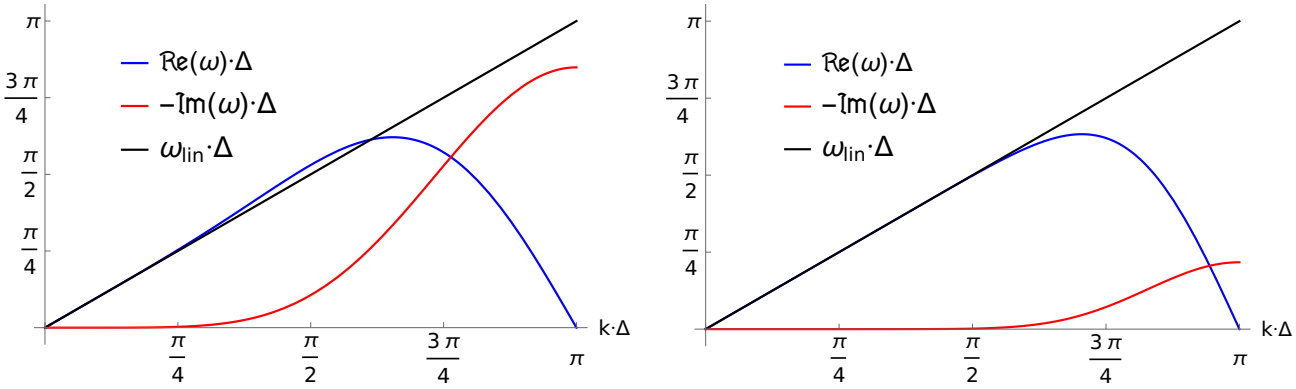

Figure 4: Plots of the real part of ω (blue), the imaginary part of ω (red) according to (55), and the linear vacuum (black), against k for asymmetric finite difference schemes of forth order (left) and thirteenth order (right). For better visibility of the symmetric plots only the values for $k \geq 0$ are shown. The trivial solution and negative frequency solutions of (55) are discarded.

It can be seen that for higher orders the real part stays close to the linear vacuum for smaller wavelengths. Higher orders also defer and decrease the rise of the imaginary part. A strong bias as in the forth order scheme (48) causes a superluminal phase-velocity in a given $k \cdot \Delta$ range. The well balanced order thirteen scheme is well behaved for a larger range of wavelengths. From figure 4, it can be deduced that the dispersion relation follows the continuous vacuum for up to $k \cdot \Delta \simeq \pi/2$. For smaller wavelengths the curve showing the real part of ω falls off from the linear vacuum and the imaginary part of ω causes a damping. Due to the concavity of the real part (in the order four scheme only for $k \cdot \Delta \gtrsim \pi/2$) there are two k's for each $\mathfrak{Re}(\omega)$. At the wavelength corresponding to the Nyquist frequency, $k \cdot \Delta = \pi$, $\mathfrak{Re}(\omega)$ becomes zero as in the cases above. The high-k values cause nonphysical standing waves, as $\mathfrak{Re}(\omega)/k \to 0$, which would cause a self-heating of the system. The damping takes care of their annihilation. The superluminosity which can be seen in the forth order finite difference differentiation is thus an acceptable add-on to the favor of a damping of nonphysical modes. Increasing accuracy and balancing as in the order 13 scheme, there is no superluminal range left.

In the numerical investigation it is demonstrated that the damping has noticeable effects already at an earlier stage than a first look at the above plot would suggest. Note that the Nyquist frequency, on the other hand, $f_{Ny} = \Delta^{-1}/2$ (corresponding to $k \cdot \Delta = \pi$), is not the limiting factor for wave modelings in this numerical scheme. It has to be stayed well below the Nyquist limit for accurately time-evolved waves. Note also that the simulation of a high frequency wave does not overshoot the Nyquist limit, as it would be sampled as a wave with lower frequency, see figure 5. The relevant frequency scale of the dispersion relation in figure 4 thus ranges only to the Nyquist limit. The algorithm is stable for any frequency.

To visualize the effects of the dispersion relation at varying wavelengths the propagation of a plane wave in a two dimensional square grid with side length $80\mu m$ divided into 1024×1024 points is investigated. The resolution is therefore given by $\Delta = 80\mu m/1024$, $\Delta^{-1} = 128 \times 10^5 m^{-1}$.

From figure 6 it can be deduced that the waves are well behaved and quite well modeled for $k \cdot \Delta \lesssim 0.5$. From figure 7, it can be inferred that already at half the Nyquist frequency the damping is non-negligible for relevant time scales. A video demonstrating the evolution on the lattice of a plane wave with a wavelength corresponding to half the Nyquist frequency can be found in the *Mendeley* repository [49]. The Nyquist frequency in this scenario is given by $f_{Ny} = 64 \times 10^5 m^{-1}$ ($\lambda = 1.5625 \times 10^{-7} m$). The conclusion is that for a proper modeling and to avoid damping effects, one is obliged to adapt the grid resolutions to the lowest wavelength such that $\Delta \lesssim 1/12\,\lambda$. While this relation is not a hard limit and can be relaxed in many cases without detriments, it poses a safe rule of thumb for long-time simulations. A sufficiently fine grid resolution is pertinent for a clean analysis of the polarization flipping and high harmonic generation effects in the present work. Since the externally provided ODE solver introduced in the next section takes care of the time integration with high accuracy, the size of a time step can be independently defined as is convenient and for the present paper varies in the range of $1fs - 6fs$, or $0.3\mu m/c - 2\mu m/c$.

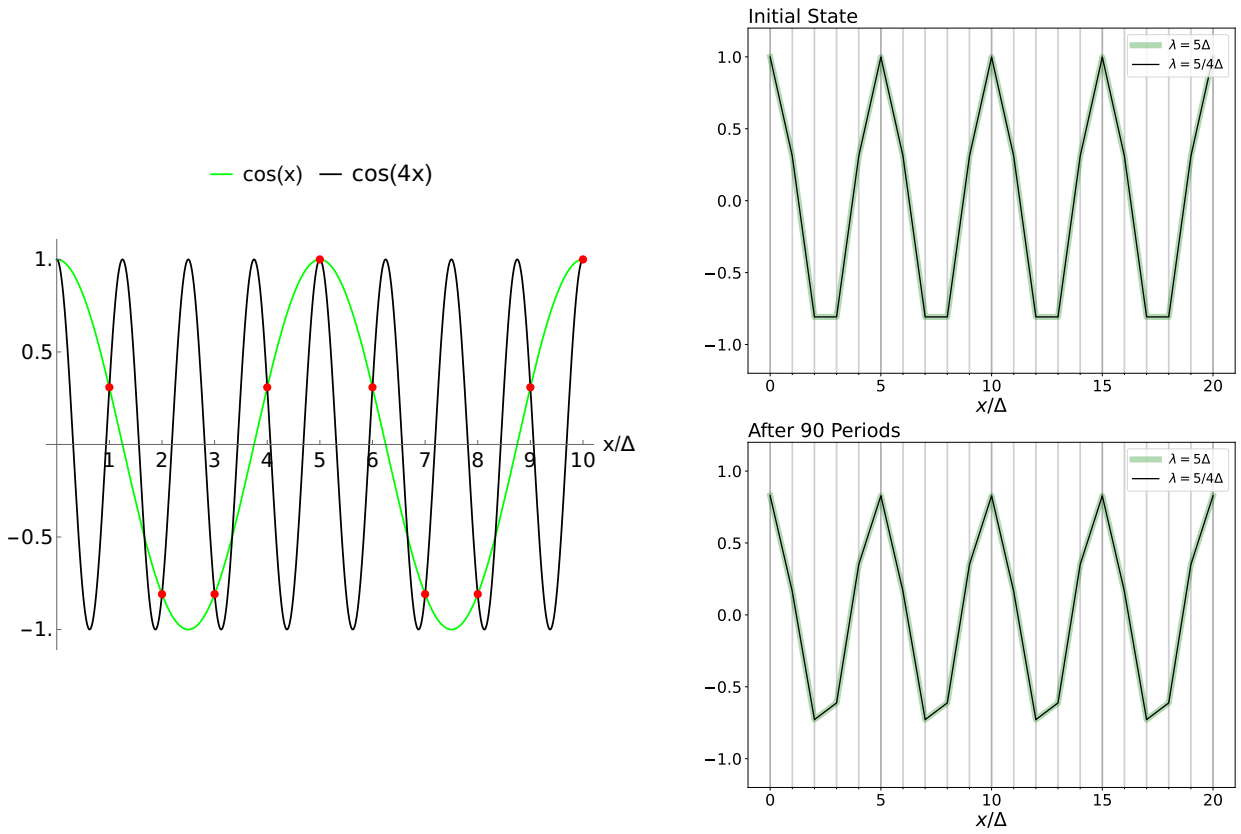

Figure 5: Effect of overshooting the Nyquist frequency. Left: Two cosine functions that when periodically evaluated at multiples of the distance $\Delta = 0.4\pi$ have the same values. Right: Simulations to verify the behavior on the grid. On a 1D line with point spacing $\Delta = 0.1\mu m$ two waves with wavelengths 5Δ and $5/4\Delta$, respectively, are simulated, corresponding to the analytical scenario on the left. It can be seen that the discretization makes no difference between the two. The simulated waves are shown in the initial state (top right) and after they have propagated the distance of 90 periods (bottom right). The damping effect due to the imaginary part of ω in the dispersion relation is the same for both waves.

5. Scaling Behavior

5.1. Solving the ODE and processing the data

For the numerical solution of the resulting nonlinear system of ODEs for $\vec{f}$ (52) the Adams-Moulton method [50] within CVODE is used, which is part of the SUNDIALS package [51]. The numerical time integration error is controllable with CVODE. By setting both relative and absolute integrator tolerances per step, the solver adapts timestep sizes according to the system's dynamics. Tolerances are set to below 10^{-12} for the present work. This yields a high accuracy while it is still well above the machine round-off error. The code writes the output data into a comma separated values (CSV) file for each user defined time step. The CSV file contains the six data columns for E_x, E_y, E_z, B_x, B_y, and B_z. Each of the six columns holds all the grid values for each of the field components. The post-processing of the data is done with the help of *Jupyter notebooks* employing the Python *SciPy* library and with the help of *Mathematica* [52–54].

5.2. Parallelization of the algorithm

For faster computation and scalability the code is parallelized. To this end the lattice is sliced, allowing separate cores to process sub-lattices. The number of sub-lattices is given by splitting each dimension of the lattice into equal parts. The finite differences used to discretize derivatives require values from neighboring sub-lattices. Hence, ghost cells are placed at the boundaries of the latter, see figure 8. The ghost cells are updated via message passing making use of *MPI* [55].

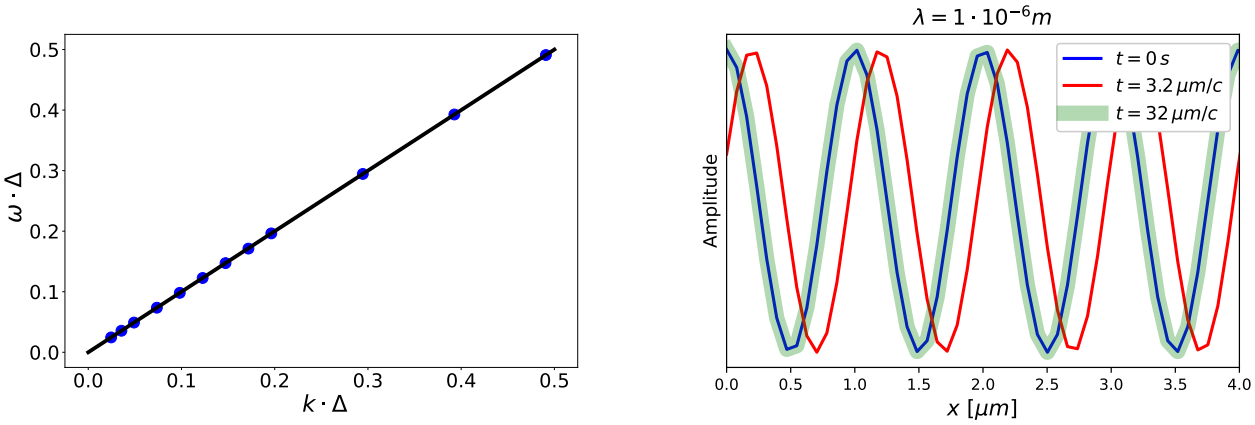

Figure 6: Left: The numerical results of the dispersion relation (blue dots) are in agreement with the free vacuum (green line) for wavelengths $20\mu m$ to $1\mu m$. The grid resolution is given by $\Delta = 80\mu m/1024$ in the propagation direction. Right: A plane wave with $\lambda = 1\mu m$ at different time steps. The wave does not lose energy – the amplitude stays the same. Even after 32 periods the waves are perfectly overlapping.

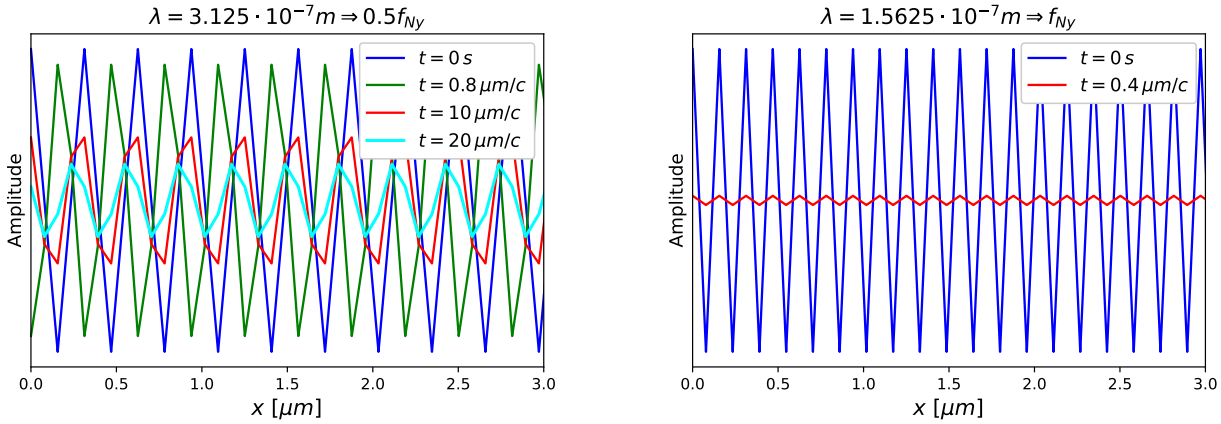

Figure 7: Left: A plane wave with $\lambda = 312.5nm$ at different time steps. The grid resolution is given by $\Delta = 80\mu m/1024$ in the propagation direction. In the free vacuum the corresponding frequency is to be associated to half the Nyquist frequency. 32 periods would have passed after 10μm/c and 62 periods after 20μm/c. The damping and also the barely sub-luminous phase velocity are, after enough propagation time, noticeable even at this wavelength. The initial peak position has clearly shifted after 20μm/c. A video showing the simulation is embedded. Right: A plane wave with $\lambda = 156.25nm$ at different time steps with the same grid settings. In the free vacuum the corresponding frequency is to be associated to the Nyquist frequency. The wave is standing and the damping is strong. The wave is quickly annihilated.

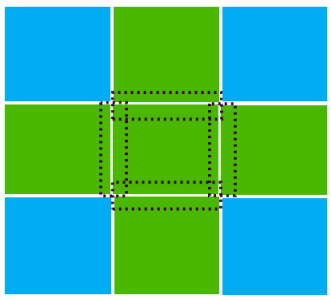

Figure 8: Ghost-cell exchange. The green square in the middle represents a sub-lattice, a batch of the interdependent grid data, being processed on one core. This process exchanges its boundary cells' values with those of the green neighboring processes. The boundary regions are indicated by the black dashes. This is done sequentially for each dimension. The blue cells at the corners do not interact with the process in the middle. The analogous situation holds in 1D and 3D.

The number of sub-lattices is equal to the size of the global MPI communicator, i.e., the number of processes. Updating a given timestep n to $n+1$ by computing the right hand side of (52) is a purely local operation. Since efficient parallelization is relevant for expensive 3D simulations a scaling test is conducted due to parallelization for the propagation of a single plane wave in a cube. To test the parallel speedup the runtimes of the code for plane wave propagation is compared for varying core number. For the test no output data is generated. The used high-performance computing (HPC) system contains 16 cores per memory domain (here a socket) and two sockets per node. The results of the scaling test are visualized in figure 9. The code is at this scale clearly memory-bound

as the behavior at the socket saturation shows.

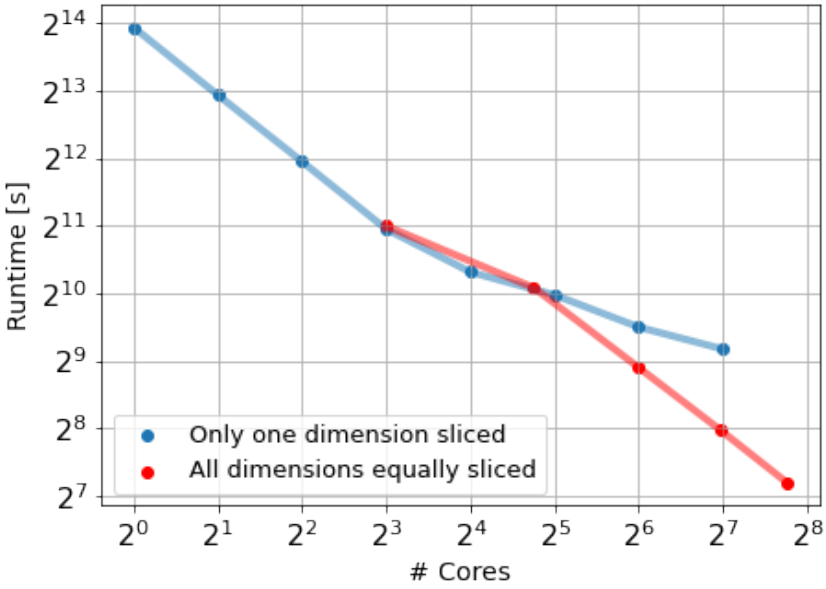

Lattice slicing only in one dimension

Number of Cores:	1	2	4	8	16	32	64	128
Average Runtime:	15692s	7838s	3960s	1979s	1273s	1006s	723s	577s

Equal slicing in every dimension

Number of Cores:	8	27	64	125	216
Average Runtime:	2041s	1083s	477s	252s	147s

Figure 9: Runtimes for the simulation of a plane wave of wavelength 4μm propagating in x-direction in a 3D cube with volume $80 \times 80 \times 80\,\mu m^3$ divided into $256 \times 256 \times 256$ lattice points. The propagation time is 100fs divided into 100 steps. Each setting is run twice and averaged in order to to take into account minor runtime variations. The runtimes nearly halve for a doubling of cores for up to 8 cores. The cube is here sliced into sub-lattices in the propagation direction of the wave (blue line and dots). The runtime speedup decreases where one memory domain (socket) is fully occupied with 16 cores. This is a typical feature for memory-bound code. The intra-socket scaling is not linear as the memory as a shared resource on the socket does not scale along with more used cores. The socket gets saturated due to memory bandwidth exhaustion when the memory interface struggles to keep up with the cores' access instructions. The cores demand more data to process than the memory interface is able to deliver. For inter-node scaling on the other hand the performance scales again along with cores and memory as parallel resources. For inter-node scaling, it can be seen that slicing only in one dimension leads to a communication overhead when the sub-lattices become too narrow. This is remedied in this scenario by an equal slicing in every dimension (red line and dots). The scaling across nodes is then again linear.

Much larger scaling tests require exclusive computing time on a number of nodes of a high-performance computing system and are part of ongoing research. At the time of writing simulations of colliding Gaussian waves in 3D with a partially revamped code run for about 13 hours on 128 cores. The configuration of these simulations are comparable to those used for 2D simulation described in section 9. For large 3D simulations like that the code becomes more and more MPI-bound. Memory requirements become very large and data sizes amount to dozens of gigabytes for single output steps. Remarkable speedups can then be achieved by merely lowering the order of the numerical scheme to four, which is still good. This is because the required depth of the ghost layers decreases from seven to three as can be seen from the biased stencils in section 4. Bottlenecks have been investigated using the Intel® oneAPI™ toolset [56]. For standard, sensible simulations the code is compute-bound in 1D, memory-bound in 2D, and MPI-bound in 3D. Communication and computation scaling is improved in ongoing research by taking advantage of hardware affinity, vectorization, MPI virtual topologies, MPI IO, hybrid OpenMP+MPI parallelization, etc.

In the next section the numerical complexity scaling of the algorithm and the employed solver with the grid size and dimension is calculated theoretically.

5.3. Computational complexity scaling of the algorithm

3D simulations run in a cube $\mathcal{C}$ with $N = N_x \cdot N_y \cdot N_z$ equally spaced points,

$$\mathcal{C} = \{x_{x,y,z} = (n_x\Delta_x, n_y\Delta_x, n_z\Delta_x) | n_i = 1, ..., N_i\} \subset \mathbb{R}^3 \ .$$

The application of the algorithm is subdivided into three computations. The calculation of the derivatives of $\vec{f}$ as well as the right hand side of the ODE (52) followed by its integration.

In the first step the derivatives are approximated by finite differences. Therefore, the number of operations does not depend on the number of lattice points. Nevertheless, the derivatives have to be performed for each point and for each dimension explicitly. For the calculation of the derivatives the computational load $\mathbf{C}_\mathrm{D}$ is obtained to be

$$\mathbf{C}_\mathrm{D} \propto D \cdot N_x \cdot N_y \cdot N_z \,,$$

where D is the number of spatial dimensions.

Second, the computation on the right hand side of (52) has to be performed for each lattice point. The dimension-dependent summation causes an extra computational load by increasing D by 1. The computational load for the calculation of (52) $\mathbf{C}_\mathrm{M}$ is given by

$$\mathbf{C}_\mathrm{M} \propto N_x \cdot N_y \cdot N_z \cdot (D+1) \,.$$

In the last step for the solution of (52) the computational load of the used ODE solver has to be taken into account. Hereby, the integration of the ODE highly depends on a wide range of considerations, such as involved frequencies or the magnitude of the nonlinearities. The computational load of the solver *CVODE* [51] $\mathbf{C}_\mathrm{S}$ is

$$\mathbf{C}_\mathrm{S} \propto N_x \cdot N_y \cdot N_z \cdot \Delta^{-1}.$$

Thus, for the upper limit of the problem with regards to the scaling behavior it is obtained

$$\mathbf{C} \propto N_x \cdot N_y \cdot N_z \cdot (D+1) \cdot \Delta^{-1} \,.$$

Next, the backtesting of the algorithm in regimes where the dispersion relation is well-behaved is performed.

6. Phase Velocity in a Strong Background

A probe plane wave is propagated along the x-axis,

$$\vec{E}(x;t) = \vec{A}\cos(kx - kvt) \,, \tag{57}$$

through a linearly polarized strong electromagnetic background field. The polarization of the strong background breaks the isotropy of space, giving rise to different refractive indices [28, 57]

$$n_\pm = 1 + \frac{\alpha}{45\pi}(11 \pm 3)\frac{E^2}{E_{cr}^2} = 1 + \delta n_\pm \tag{58}$$

for a probe polarization orthogonal (+) and parallel (-) to the background polarization. Since (58) only takes into account the 4-photon interaction contribution, i.e., it neglects all but the first nonlinear term in (7), the results are verified turning off 6-photon processes in the simulations.

The phase shift caused by the nonlinear deviation from the vacuum speed of light is given by

$$v \to \frac{1}{1+\delta n_\pm} \Rightarrow v_\mathrm{nli} = -\frac{\delta n_\pm}{1+\delta n_\pm} \,. \tag{59}$$

Its contribution to the phase can be extracted by a Fourier analysis of the time-propagated wave. When the passed time of propagation is chosen to be an integer multiple of λ, it is obtained with $l \in \mathbb{N}$ [39]

$$\vec{E}(x; l\cdot t) = \vec{A}\cos(2\pi x/\lambda - 2\pi l\, v_\mathrm{nli}) = \vec{A}\cos(2\pi(x/\lambda - l\, v_\mathrm{nli})) \,. \tag{60}$$

The nonlinear phase value contribution can then be extracted from the phase after a spatial Fourier transformation evaluated at $1/\lambda$. This results in

$$v_\mathrm{nli} = -\frac{1}{2\pi l}\,\arg\left(\mathrm{FT}[E(x;t_l)](\lambda^{-1})\right) \quad \text{with} \quad t_l = l\cdot\lambda. \tag{61}$$

The spatial Fourier transform of (61) can be replaced by a fast Fourier transform in the analysis.

To analyze the phase velocity variation numerically the background field strength is varied. In a second step the relative polarization of the waves is changed from parallel to orthogonal. The configurations are given in table 1. The total simulation time is chosen to be $200\mu m/c$, conveniently divided into 100 steps of $2\mu m$ – the chosen wavelength of the probe wave.

Table 1: Settings for phase velocity variation tests.
The background amplitudes and the relative polarization are varied. The large wavelength of the background manifests itself as an ever-persistent static background.

Grid	Length	$100\mu m$
	Lattice Points	1000
Background	$\vec{A}_b$	(0,60,0)μE_{cr} up to (0,1.5,0)E_{cr}
	λ	$1Pm$
Probe	$\vec{A}_p$	(0,1,0) and (0,0,1)μE_{cr}
	λ	$2\mu m$

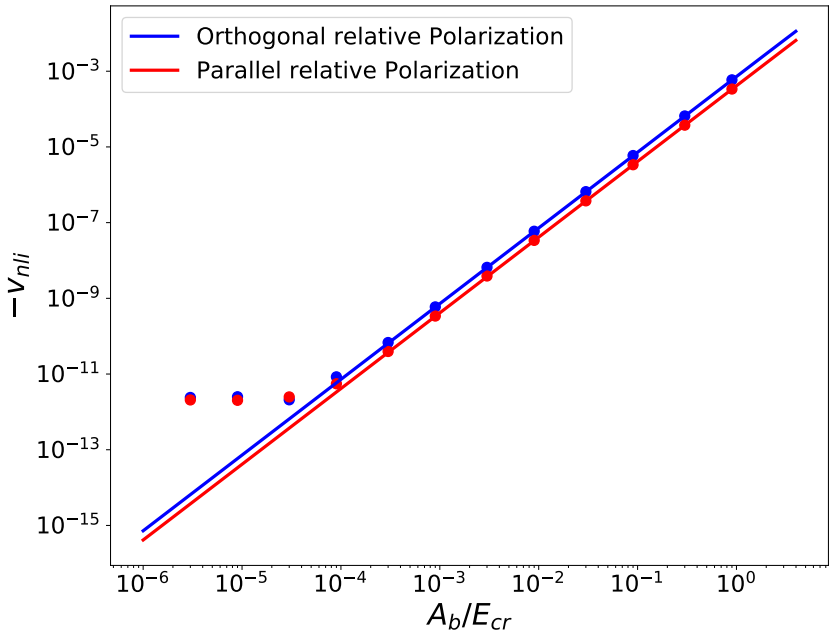

Figure 10: Nonlinear contribution to the phase velocity slow-down in a background with varying field strength. The results converge to a value $\approx 2 \times 10^{-12}$ for small background field strengths. This is the phase velocity reduction caused by the lattice itself due to numerical errors. This numerical effect is getting larger than the physical effect for $A_b < 10^{-4} E_{cr}$. The values for background field strengths larger than $5 \times 10^{-4} E_{cr}$ have a mean absolute percentage error of 1.8% for parallel relative polarization and 1.2% for orthogonal relative polarization. The first error is presumably larger since the probe wave is not a perfect "probe" and contributes with its own polarization.

It can be seen that the nonlinear interactions give note to themselves in a reduction of the phase velocity of the simulated waves in figure 10. For sufficiently large background field strengths the numerical values are in perfect agreement with the analytical predictions.

7. Polarization Flipping – Vacuum Birefringence

Polarization or helicity flipping of a probe pulse propagating through a strong pump pulse is a result of vacuum birefringence. The origin of the effect is again the breaking of the isotropy of space by the polarization of the strong background. The refractive indices from above

$$n_- = 1 + \frac{8\alpha}{45\pi}\frac{E^2}{E_{cr}^2} \quad \text{and} \quad n_+ = 1 + \frac{14\alpha}{45\pi}\frac{E^2}{E_{cr}^2} \tag{62}$$

generate a difference in optical path length for the probe pulse polarization components parallel and orthogonal to the pump polarization which results in *bi*refringence. On a microscopic level, a portion of the pulse's quanta flip their polarization. Macroscopically, the overall polarization experiences a tiny turn.

A typical probe-pump scenario devised for the observation of helicity flips is shown in figure 11. A probe pulse in the x-ray regime propagates through a strong low-frequency pump field in which spatial isotropy is broken. A corresponding simulation configuration showing one polarization direction is shown in figure 12.

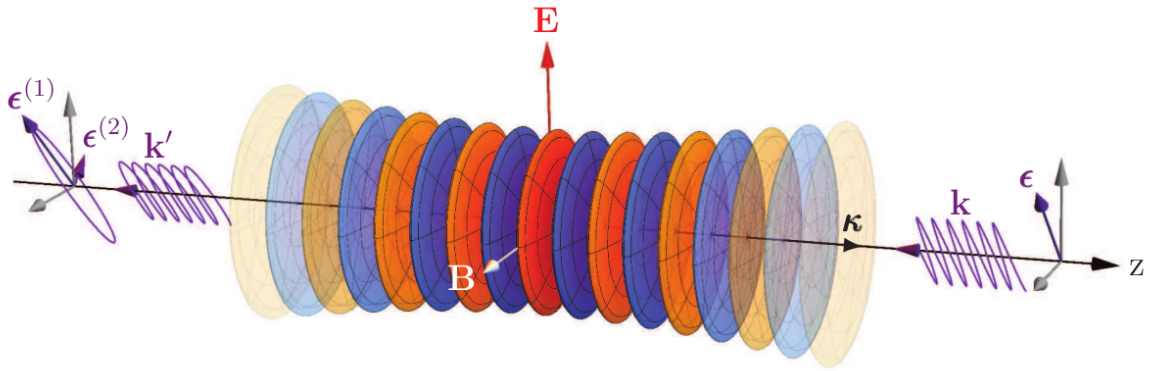

Figure 11: Sketch of the pump-probe type scenario intended to verify vacuum birefringence. A linearly polarized optical high-intensity laser pulse – wavevector κ, electric (magnetic) field $\mathbf{E}$ ($\mathbf{B}$) – propagates along the positive z-axis. Its strong electromagnetic field couples to the charged particle-antiparticle fluctuations in the quantum vacuum, and thereby effectively modifies its properties to be probed by a counter-propagating x-ray beam (wavevector k, polarization ϵ). Vacuum birefringence manifests itself in an ellipticity of the outgoing x-ray photons (wavevector k', polarization components along $\epsilon^{(1)}$ and $\epsilon^{(2)}$). Figure and caption taken from [27].

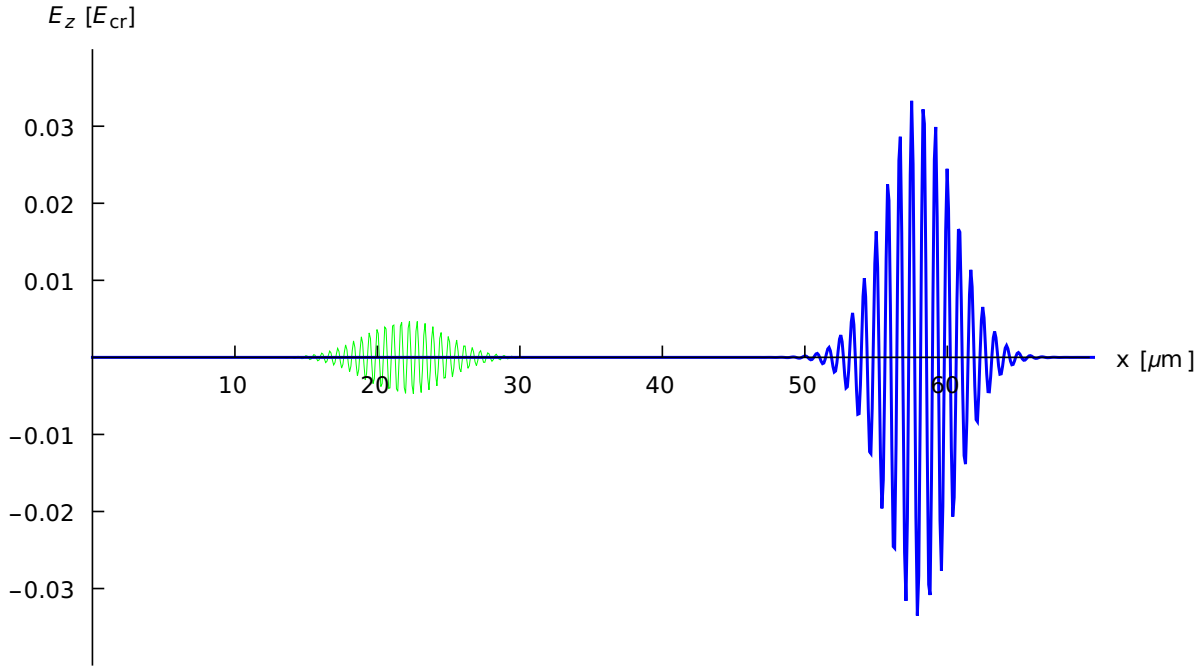

Figure 12: Sketch of the pulse configuration for the simulation of polarization flipping. On the left is the weak probe pulse which propagates to the right and on the right is the strong pump pulse propagating leftwards. Note that in actual simulations (table 2) the probe field strength and wavelength are much smaller. Adjustments are here for better visibility.

In order to backtest the numerical solver, firstly (subsection 7.1), parametric checks of the flipping probability as derived in [28] are performed. The settings given in table 2 are chosen to this end with Gaussian pulses given by (64) below. With that result being verified, secondly (subsection 7.2), the scaling properties are made use of to attain the analytical result of a real-life calculation for a polarization flipping scenario calculated in [27]. The parameters for that setup are listed in table 3.

For both cases the normalized vectors parallel and orthogonal to the initial probe polarization are given as

$$\vec{\varepsilon}_{\parallel} = (0, 1/\sqrt{2}, 1/\sqrt{2}) \quad \text{and} \quad \vec{\varepsilon}_{\perp} = (0, -1/\sqrt{2}, 1/\sqrt{2})\,. \tag{63}$$

For the simulations 1D Gaussian pulses are used in the form

$$\vec{E} = \vec{A}\, e^{-(\vec{x}-\vec{x}_0)^2/\tau^2} \cos(\vec{k}\cdot\vec{x})\,. \tag{64}$$

The vector $\vec{A}$ comprises amplitude and polarization, $\vec{x}_0$ is the center of the pulse, τ its width, and $\vec{k}$ the wavevector. For convenience, the normalized vector $\hat{k}$ giving the propagation direction is stated in the parameter tables. As pulses are simulated instead of single photon quanta the number of flipped photons is obtained via the pulse energies

$$\frac{N_\perp}{N} = \frac{\hbar\omega N_\perp}{\hbar\omega N} = \frac{\mathrm{E}_\perp}{\mathrm{E}_{tot}}\,, \tag{65}$$

where the energies in the respective polarization directions are proportional to the electric field strength projections squared

$$\mathrm{E}_\perp \sim \sum_{x_i \in \mathcal{C}} \left(\vec{E}(x_i) \cdot \vec{\varepsilon}_\perp \right)^2 , \quad \mathrm{E}_\parallel \sim \sum_{x_i \in \mathcal{C}} \left(\vec{E}(x_i) \cdot \vec{\varepsilon}_\parallel \right)^2 , \quad \mathrm{E}_{tot} = \mathrm{E}_\perp + \mathrm{E}_\parallel \ . \tag{66}$$

All other factors in (65) cancel.

7.1. Vacuum birefringence – parametrical dependencies

For coaxially counterpropagating unfocused pump and probe pulses the polarization flip probability, taking into account again only up to 4-photon interactions, in the low-energy approximation for a plane wave pump field is given by [28]

$$P_{\text{flip}} = \frac{\alpha^2}{255 \lambda_{\text{probe}}^2} \sin^2(2\sigma) \left(\int dx \frac{E_{\text{pump}}(x)^2}{E_{cr}^2} \right)^2 , \tag{67}$$

where σ is the angle between the probe and pump polarizations. The probe field strength is assumed to be negligible compared to the pump. The probability directly translates to the flip ratio

$$N_\perp = P_{\text{flip}} \cdot N \ . \tag{68}$$

Formula (67) yields all the parametric dependencies for the probability of polarization flips and indirectly excludes other parameters. Note the strong dependence on the pump field strength and also on the probe wavelength. Notably, it is independent of the shape of the pulses. Deviations from the above formula for focused background pulses is discussed in the next subsection. In 1D simulations the background can be modeled as a Gaussian. To investigate the scaling properties of the numerical solver the settings in table 2 are used. A time-resolved flipping process for those parameters is depicted in figure 13. The results of the scaling tests are visualized in figure 14. There is perfect agreement between the 1D simulation results and formula (67). With these scaling properties being verified in the algorithm, in the following subsection the analytical result in case (a) of [27] is reproduced with the use of extrapolations.

Table 2: Parameters for probe and pulse beams chosen to check the parametric dependencies in (67).
The peak to peak distance at $t = 0$ is 36 μm. The probe wavelength, the pump field strength, and their relative polarization are varied to obtain the parametric dependencies in figure 14.

Grid	Length	$80\mu m$
	Lattice Points	60000
Pump	$\vec{A}$	$(0,0,34)\mathrm{m}E_{cr}$
	$\hat{k}$	(-1,0,0)
	λ	$800nm$
	$\vec{x}_0$	$58\mu m$
	τ	$3.5\mu m$
Probe	$\vec{A}$	$(0,50,50)\mu E_{cr}$
	$\hat{k}$	(1,0,0)
	λ	$25nm$
	$\vec{x}_0$	$22\mu m$
	τ	$4.0\mu m$

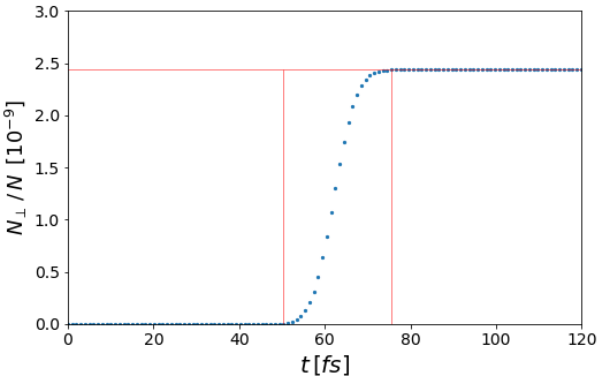

Figure 13: Time evolution of the polarization flipping ratio for the parameters presented in table 2. A simulation time of $30\mu m$ divided into 100 steps, so $1fs$ per step is used. The distance between the vertical lines is the total interaction time t_I=25fs. The settings used here provide an interaction time of 25fs, indicated by the red vertical lines. The red horizontal line corresponds to the asymptotic relative flip ratio.

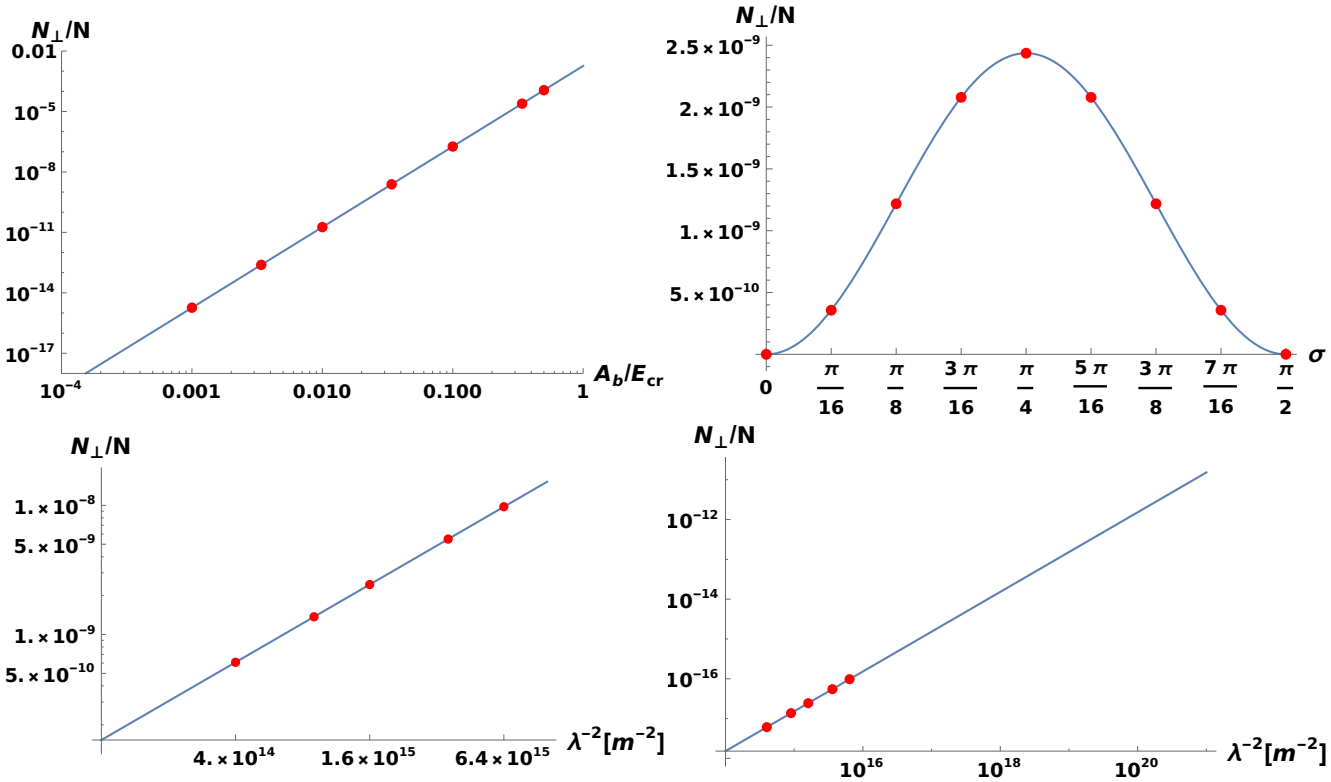

Figure 14: Scaling of the polarization flipping probability with variations of the parameters given in table 2. The solid lines are obtained with (67). The red dots are simulation results. Top left: Varying the background field strength. Top right: Varying the relative polarization angle of probe and pump. Bottom left: Varying the probe wavelength. Bottom right: Combining the scaling of the pump field strength and probe wavelength – A_b is scaled down by a factor 100 compared to 2. Simultaneously an extrapolation to frequencies in the x-ray regime is performed. This last way of combining scaling properties is useful in order to extrapolate to relevant probe frequency scales while keeping the numerical accuracy high and the computational load low.

It has to be noted here, as it has also been found in [39], that there is a signal at $\sigma = \pi/2$ in the top right diagram of figure 14 with value 2.87×10^{-14}. This is above the numerical noise and due to harmonic generation. The polarization of a harmonic resulting from a higher order photon interaction is determined by energy conservation to be along the polarization of the pulse contributing with an uneven amount of photons. Hence, even though there should be no signal from polarization flipping, there are signals from harmonic generation. Harmonic generation is however not considered in formula (67). This example shows that the simulation algorithm yields all effects in one go in contrast to most analytical calculations. Combined effects like this are up to future research where the algorithmic solver will hopefully prove invaluable. Neglecting that signal, the mean absolute percentage errors in all the scaling plots above are below 0.1%.

7.2. Vacuum birefringence – extrapolation to an analytical value in the x-ray regime

The settings for the simulation of the scenario described in case (a) in [27] are given in table 3. For this real-life 3D scenario the techniques have to be adapted. First, the pump field strength is too low to extract the flipping process from the numerical noise. To combat this, it is being made use of the field strength scaling properties. Second, the chosen probe frequency is very high. An extremely fine grid would be necessary to model that pulse. To evade computations that expensive, the wavelength scaling properties can be made use of. It is thus a combination of two scaling methods in the way shown in the bottom right of figure 14 and described in that caption.

Besides that, the 1D simulations do not take into account lateral dispersion (diffusion) effects of the focused background field as they are present in 3D. That deficiency is remedied by reducing the pump peak field strength to the average over the interaction time $t_I \simeq 23.5fs$, see figure 15. The pump peak amplitude is thereby reduced from $0.34\text{m}E_{cr}$ to $0.29\text{m}E_{cr}$. This is a source of errors, especially when used for an extrapolation over several orders of magnitude. The results in figure 16 show that the extrapolation in principle works. The extrapolated value is 1.44×10^{-12} while the result in [27] is 1.39×10^{-12}.

Table 3: Parameters for probe and pulse beam adapted to [27].
The pump field strength is obtained as the square root of the ratio of intensity to critical intensity. Pump and probe are coaxially counterpropagating. The pulse durations are $30fs$. Furthermore, pump and probe polarizations are at an angle of $\pi/4$ and the initial peak to peak distance is $36\,\mu m$.

Grid	Length	$80\mu m$
	Lattice Points	40000
Pump	$\vec{A}$	$(0,0,0.34)\mathrm{m}E_{cr}$
	$\hat{k}$	(-1,0,0)
	λ	$800nm$
	$\vec{x}_0$	$58\mu m$
	τ	$4.5\mu m$
Probe	$\vec{A}$	$(0,50,50)\mu E_{cr}$
	$\hat{k}$	(1,0,0)
	λ	$96pm$
	$\vec{x}_0$	$22\mu m$
	τ	$3.4\mu m$

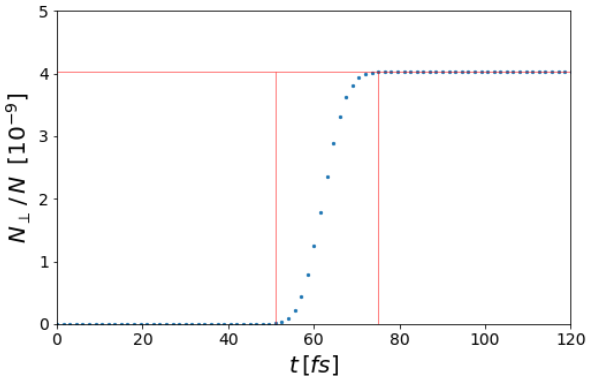

Figure 15: Time evolution of the polarization flip probability for an adaptation of the parameters presented in table 3. One time step corresponds to $1.5fs$. The adaptations are: The pump field strength is magnified by a factor 100 to $34\mathrm{m}E_{cr}$ in order to reduce numerical noise. The probe wavelength is enlarged to the computationally acceptable value of 25nm. The distance between the vertical red lines is the total interaction time t_I=24fs. The horizontal red line denotes the asymptotic relative flip ratio.

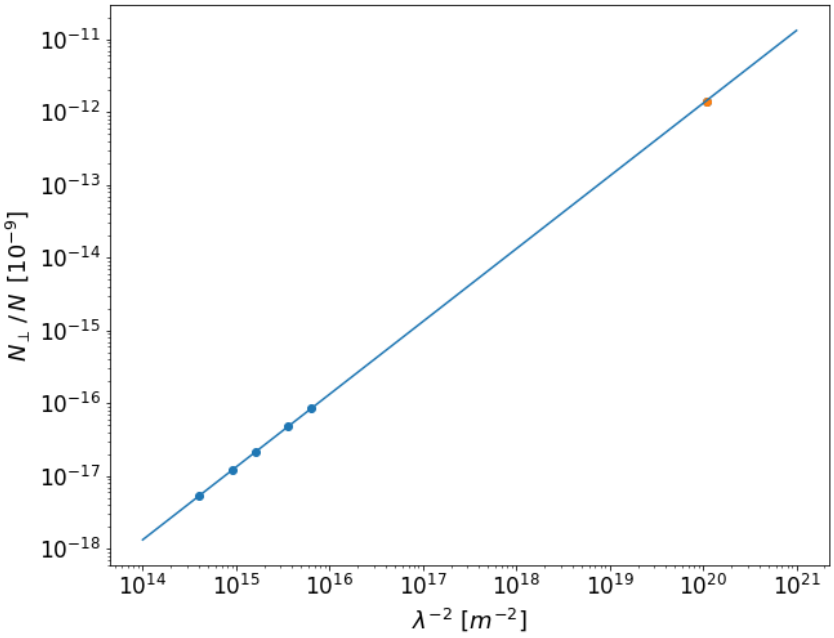

Figure 16: Extrapolation of polarization flipping ratios to high frequencies in 3D by emulating diffusion in 1D simulations.
The blue line is an extrapolation of simulation results with various probe wavelengths (blue dots). The orange dot represents the value obtained in [27].

8. High Harmonic Generation

To backtest the algorithmic program the prominent scenario for the detection of nonlinear vacuum signatures shown in figure 17 is considered again. For the present analysis two head-on colliding pulses are assumed, a weak probe pulse and a strong zero-frequency background pulse. The initial settings are listed in table 4.

Approximate analytical results for this scenario have been derived in [15, 17]. The effective vertices for 4- and 6-photon scattering in figure 18 (a) can produce higher-frequency outgoing photons by photon merging. As an example, in figure 18 (b) two probe photons and a zero-frequency background photon merge into an outgoing photon with frequency $2\omega_p$.

Table 4: Initial settings to observe harmonic generation in 1D simulations, see figure 17.

Grid	Length	$300\mu m$
	Lattice Points	4000
Pump	$\vec{A}$	$(0,20,0)\mathrm{m}E_{cr}$
	$\hat{k}$	(-1,0,0)
	λ	$1m$
	x_0	$200\mu m$
	τ	$12.8\mu m$
Probe	$\vec{A}$	$(0,5,0)\mathrm{m}E_{cr}$
	$\hat{k}$	(1,0,0)
	λ	$2\mu m$
	x_0	$100\mu m$
	τ	$10\mu m$

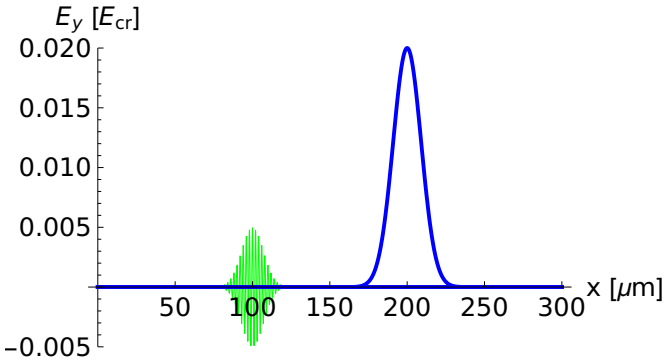

Figure 17: Visualization of the pulse configuration to detect higher harmonics with a zero-frequency background pulse, see table 4.

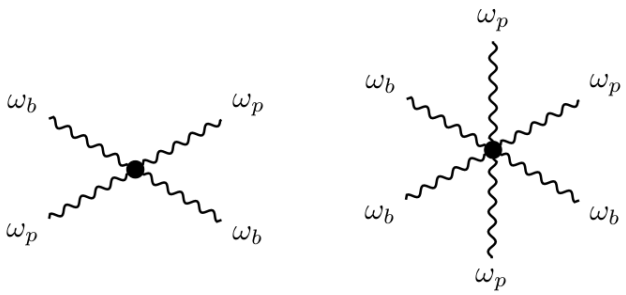

(a) Effective vertices for 4- and 6-photon scattering

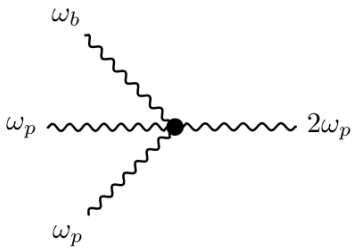

(b) High harmonic generation with a zero-frequency background

Figure 18: Feynman diagrams for harmonic generation. In (b) there is an implicit time axis from left to right.

The possible contributions of two wave scattering resulting from the the weak-field expansion are depicted in figure 19.

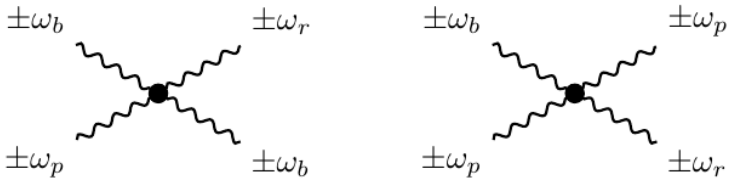

(a) $\omega_r \in \omega_b, 2\omega_p \pm w_b, \omega_p, \omega_p \pm 2\omega_b$

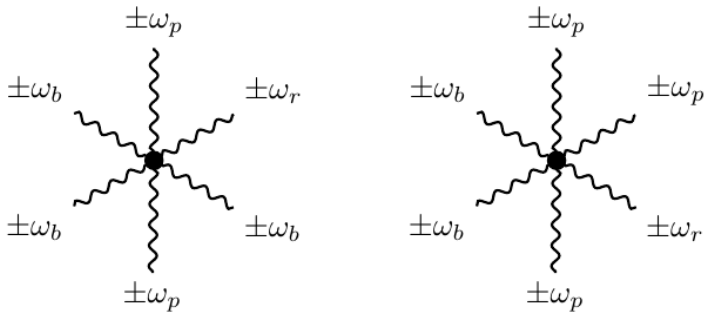

(b) $w_r \in \omega_b, 3\omega_b, \omega_p + 3\omega_b, 2\omega_p \mp 2\omega_b, \omega_p, \omega_p \mp 2\omega_b, 3\omega_p \mp 2\omega_b$

Figure 19: Allowed vertices and resulting frequencies ω_r for harmonic generation with 4-photon (a) and 6-photon (b) processes [15]. Further restrictions are posed upon the asymptotic states by energy conservation.

In the present case of $\omega_b = 0$ it is found for

4-photon processes:

- The scattering of a background and a probe photon contributes with one photon to the zeroth harmonic ($\omega = 0$) and with one to the fundamental harmonic ($\omega = \omega_p$).
- Two background photons and one probe photon merge and produce a photon of the fundamental harmonic ($\omega = \omega_p$).
- Two probe photons and one background photon merge and produce a photon of the second harmonic ($\omega = 2\omega_p$).

6-photon processes:

- The sheer scattering of background and probe photons contributes to the zeroth harmonic and the fundamental harmonic.
- Two background and two probe photons merge and produce one photon contributing to the second harmonic and one contributing to the zeroth harmonic.
- Two background and two probe photons merge and produce two photons contributing to the fundamental harmonic.
- Two background photons and three probe photons merge and produce a photon contributing to the third harmonic ($\omega = 3\omega_p$).
- The merging of three background and two probe photons produces a photon contributing to the second harmonic.

A visualization of the contributions is provided with figure 21. It can be seen that the asymptotic contribution to the second harmonic is only due to 6-photon processes. That is because wave-mixing – resulting pulses that are combined of photons of both pulses – is asymptotically not allowed. This is due to energy conservation for coaxial pulses, as for a photon resulting of wave-mixing the following holds:

$$k^\mu_{\text{res}} = n_p\,\omega_p\,(1,\hat{k}) + n_b\,\omega_b\,(1,-\hat{k}) \quad \text{and} \quad (k^\mu_{\text{res}})^2 = 0 \;\Rightarrow n_p\,n_b \overset{!}{=} 0\ , \tag{69}$$

where n_p and n_b are the numbers of the contributing photons and $\hat{k}$ is the normalized propagation direction vector of the probe pulse. These states are thus only visible in the overlap configuration. The 6-photon process, on the other hand, can produce second harmonics without wave-mixing, see the second point for six-photon processes above. For the highest generated harmonic, the short-lived third harmonic, the rule-of-thumb resolution limit for the grid defined in the end of section 4 is slightly exceeded. This comes without noticeable accuracy problems as is shown in the next subsections.

8.1. High harmonic generation – analytical results

Analytical methods in [15, 17] contain a derivation of iterative solutions to the nonlinear equations of motion for zero-frequency backgrounds. With the probe (p) and background (b) pulses as time-dependent 1D Gaussians with the parameters of table 4 the Gaussians are obtained to be, compared to (64),

$$\vec{E}_p(x;t) = \vec{\epsilon}_p\,A_p\,e^{-(k^\mu_p x_{\mu p})^2/(\omega_p\tau_p)^2}\cos(k^\mu_p x_{\mu p}) \quad \text{and} \quad \vec{E}_b(x;t) = \vec{\epsilon}_b\,A_b\,e^{-(k^\mu_b x_{\mu b})^2/(\omega_b\tau_b)^2}\ , \tag{70}$$

with $k^\mu_j x_{j\mu} = \omega_j t - \vec{k}_j\vec{x}_j$. The shifted coordinates of probe and background field read

$$\vec{x}_p = (x - 100\mu m, 0, 0) \quad \text{and} \quad \vec{x}_b = (x - 200\mu m, 0, 0)\ . \tag{71}$$

Writing a combined electric field as

$$\vec{E} = \vec{E}_p + \vec{E}_b\ , \tag{72}$$

the inhomogeneous wave equation in 1D can be written as

$$(\partial_t^2 - \partial_x^2)\,\vec{E} = T[\vec{E}]\ . \tag{73}$$

The source term T comprises the nonlinear Heisenberg-Euler interactions. Decomposing the electric field into

$$\vec{E} = \vec{E}^{(0)} + \vec{E}^{(1)} + ...\ , \tag{74}$$

where $\vec{E}^{(0)}$ solves the free vacuum wave equation $(\partial_t^2 - \partial_x^2)\,\vec{E}^{(0)} = 0$, an iterative procedure is obtained [15] in which

$$(\partial_t^2 - \partial_x^2)\,\vec{E}^{(1)} = T[\vec{E}^{(0)}]\ . \tag{75}$$

With the polarization for both fields given by

$$\vec{\epsilon} = (0, 1, 0) \tag{76}$$

and defining the shorthands

$$\kappa_p = \frac{k_p^\mu x_{\mu p}}{\omega_p \tau_p} \quad \text{and} \quad \kappa_b = \frac{k_b^\mu x_{\mu b}}{\omega_b \tau_b} \ , \tag{77}$$

it is then obtained for the solution to the nonlinear wave equation (75) at the first iterative order for

- the dc component (zeroth harmonic):
  The overlap field

$$\vec{E}_{0,o}^{(1)} = -\frac{8\alpha}{180\pi} A_p^2 \, \vec{E}_b(x;t) \, e^{-2\kappa_p^2} \, \vec{\epsilon} \tag{78}$$

  and the asymptotic field

$$\vec{E}_{0,a}^{(1)} = \frac{8\alpha}{180\pi} A_p^2 \sqrt{\frac{\pi}{2}} \, \frac{\tau_p \kappa_b}{\tau_b} (1 + \mathrm{erf}(\sqrt{2}\kappa_b)) \, A_b \, e^{-\kappa_b^2} \, \vec{\epsilon} \, . \tag{79}$$

- the fundamental harmonic (first harmonic):
  The overlap field

$$\vec{E}_{1,o}^{(1)} = -\frac{8\alpha}{90\pi} A_p e^{-\kappa_p^2} \, \vec{E}_b(x;t)^2 \, \cos(k_p^\mu x_{p\mu}) \, \vec{\epsilon} \tag{80}$$

  and the asymptotic field

$$\vec{E}_{1,a}^{(1)} = \frac{8\alpha}{90\pi} A_p e^{-\kappa_p^2} A_b^2 \sqrt{\frac{\pi}{2}} \omega_p \tau_b \, \frac{1 + \mathrm{erf}(\sqrt{2}\kappa_b)}{2} \, \sin(k_p^\mu x_{p\mu}) \, \vec{\epsilon} \, . \tag{81}$$

- the second harmonic:
  The overlap field

$$\vec{E}_{2,o}^{(1)} = -A_p^2 e^{-2\kappa_p^2} \left[\frac{8\alpha}{180\pi} \, \vec{E}_b(x;t)^2 \, + \frac{96\alpha}{630\pi} \, \vec{E}_b(x;t)^3 \right] \cos(2k_p^\mu x_{p\mu}) \, \vec{\epsilon} \tag{82}$$

  and the asymptotic field

$$\vec{E}_{2,a}^{(1)} = \frac{96\alpha}{315\pi} A_p^2 e^{-2\kappa_p^2} A_b^3 \sqrt{\frac{\pi}{3}} \omega_p \tau_b \, \frac{1 + \mathrm{erf}(\sqrt{3}\kappa_b)}{2} \, \sin(2k_p^\mu x_{p\mu}) \, \vec{\epsilon} \, . \tag{83}$$

- the third harmonic:
  The overlap field

$$\vec{E}_{3,o}^{(1)} = -\frac{96\alpha}{1260\pi} A_p^3 e^{-3\kappa_p^2} \, \vec{E}_b(x;t)^2 \, \cos(3k_p^\mu x_{p\mu}) \, \vec{\epsilon} \tag{84}$$

  and the asymptotic field

$$\vec{E}_{3,a}^{(1)} = 0 \ . \tag{85}$$

Using the values from table 4 the solid blue transparent lines in figure 22 are obtained. Those are employed to scrutinize the correctness of the simulations. Animations of the arising and the evolution of the various harmonics are provided in the *Mendeley* repository [49] (thumbnails and description in figure 20).

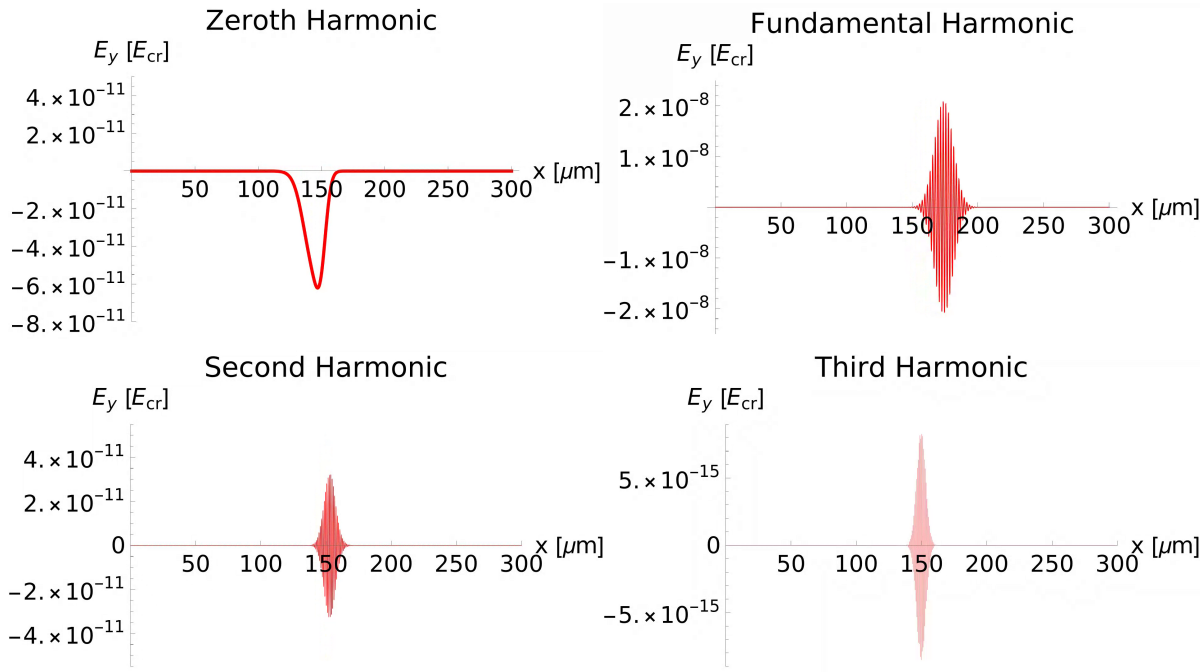

Figure 20: Thumbnails of animations available in the *Mendeley* repository [49] showing the time evolution of the various harmonics in 1D due to a pulse collision with the specification of 4 with nonlinear 4-photon and 6-photon interactions. Zeroth harmonic (top left), first harmonic (top right), second harmonic (bottom left), and third harmonic (bottom right).

8.2. High harmonic generation – simulation results

The interest lies predominantly in the nonlinear contributions to the generation of harmonics. Therefore, each setting is simulated three times with varying combinations of interactions included. Once including only the nonlinear effects of four- and six-photon contributions. Once including only six-photon processes. Once excluding all nonlinear interactions, i.e., only the linear vacuum. By subtracting the dynamics in the linear vacuum from the nonlinear dynamics the higher order processes of the weak-field expansion are extracted. The simulations of six-photon processes permit to isolate their sole contribution, see figure 21. It is a nice feature of the simulation code that the contributions of 4- and 6-photon diagrams can be turned on and off to make them separately visible.

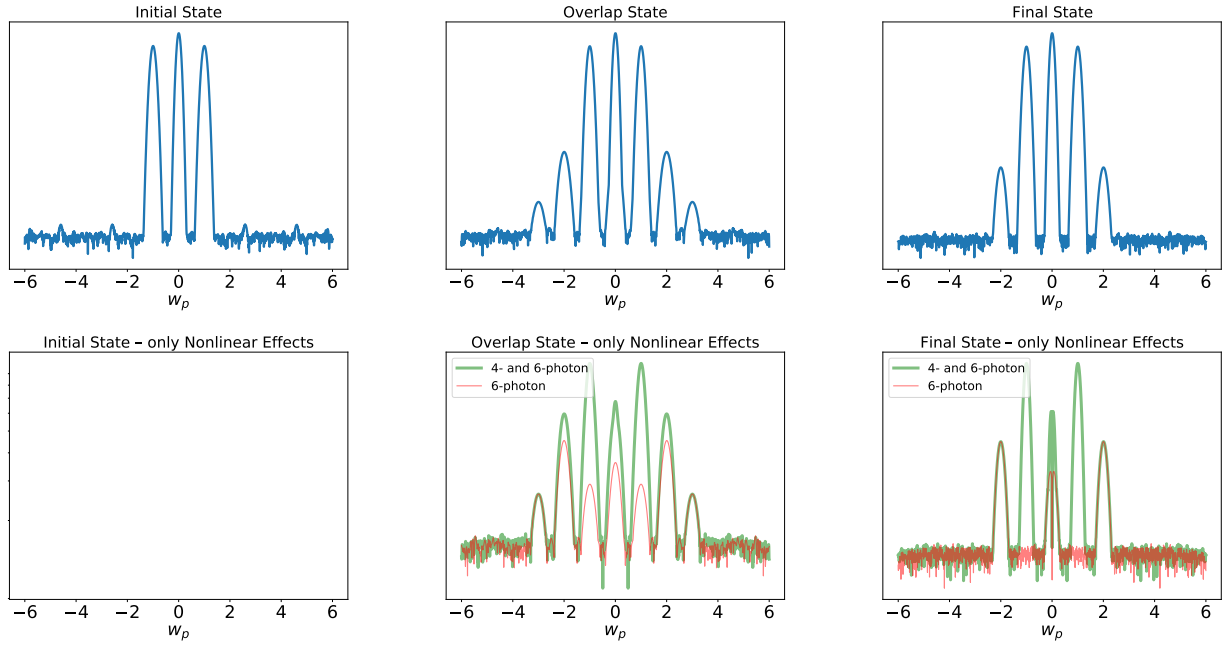

Figure 21: A log scale makes the higher harmonics visible in frequency space. Top: a full simulation of the linear vacuum supplemented by 4- and 6-photon nonlinear interactions. Bottom: after subtraction of the linear vacuum. The initial state contains only the main signals that disappear without the linear terms. The overlap state is the time step where the pulses are directly overlapping, at the final state they have separated again – the asymptotic field is left. It can be deduced that the third harmonic and the asymptotic part of the second harmonic are only due to 6-photon processes.

In order to extract the amplitudes of the various arising harmonics and their time evolution, their respective frequencies have to be filtered in Fourier space by setting all others to zero and then transforming back to position

space [39]. The amplitude is obtained directly as the maximum norm and its time evolution can be observed. A time step in these simulations is $1\mu m/c$. The results for the zeroth harmonic (dc component), first harmonic (fundamental harmonic), second, and third harmonic are shown in figure 22.

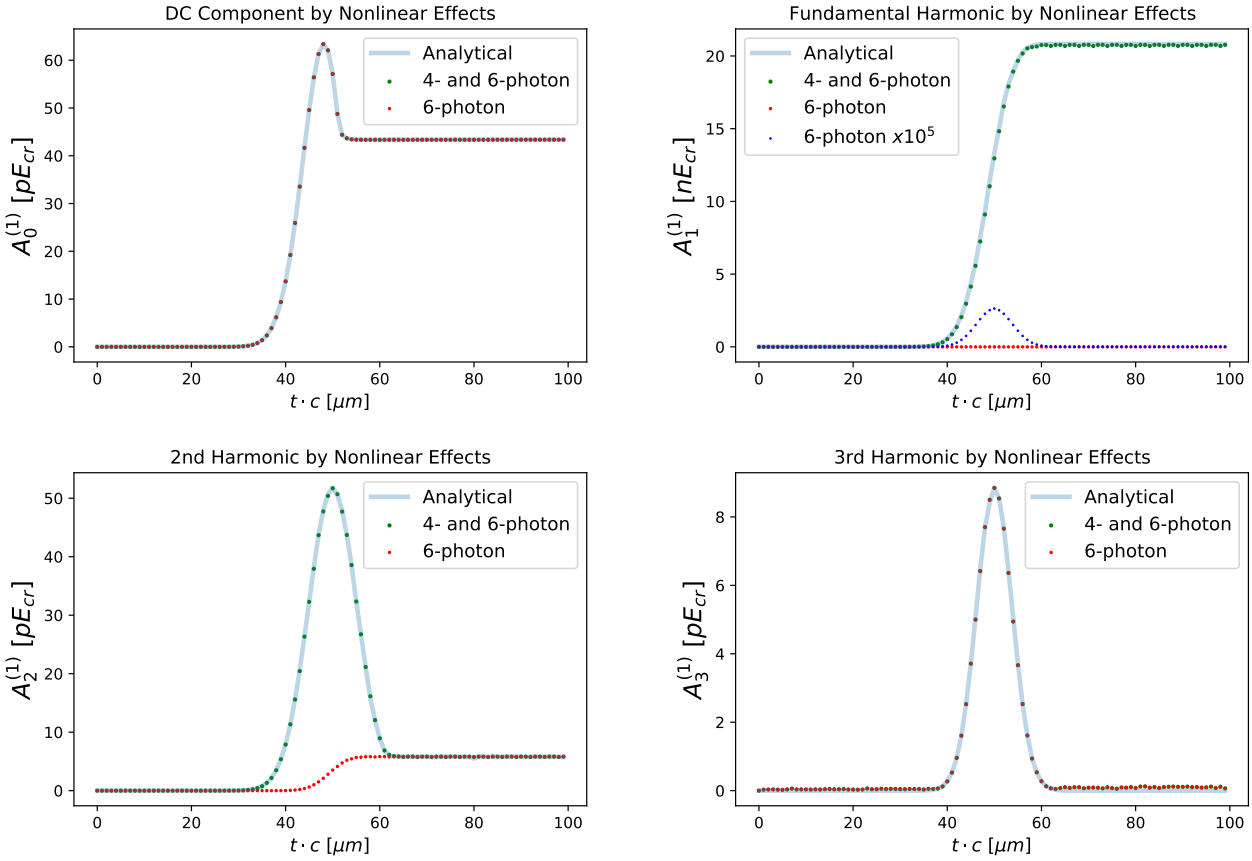

Figure 22: Amplitude evolution of the harmonics caused by 4- and 6-photon processes combined and only by 6-photon processes after subtraction of the linear vacuum propagation. Dots in brown (color overlap of green and red) indicate an overlap of 6-photon processes with the combined values for 4- and 6-photon processes. Analytical approximations obtained in (78)-(85) are underlying as the blue transparent curve.

As can be seen in figure 22 there is good agreement between the analytical approximation and the simulation results. There small are systematic errors due to the back and forth Fourier transformation and slicing of frequency ranges. The mean absolute percentage errors of the simulation results are calculated to be less than 1% in the regions where the amplitudes are non-vanishing.

Asymptotic states are constrained by energy-momentum conservation, while the overlap state has a richer spectrum. This spectrum becomes especially versatile when the pulses collide at a non-zero angle, which is a task for future work of higher-dimensional simulations. First results are demonstrated in section 9.

In the next section and subsequent works, the zero-frequency background restriction is relaxed and the pulses collide at a non-zero angle. Signals which are degenerate in the case of a one zero-frequency pulse split up. Simulations in higher dimensions provide a means to analyze varying collision configurations. Situations that pose no further difficulty to the code are considerably hard to cope with analytically. Employing simulations of this algorithm it is possible to track harmonic frequencies in time and space for scenarios of arbitrary pulse parameters – with the only restrictions posed by the applicability of the Heisenberg-Euler weak-field expansion and computational feasibility.

9. 2D Simulations

For simulations in 2D a special adaptation of 3D Gaussian pulses is used to model the diffusion behavior. The pulse propagates along $z(t) = t - z$. The beam waist of the pulse at position z is given by

$$w(z) = w_0 \sqrt{1 + \left(\frac{z - z_0}{z_R} \right)^2} \tag{86}$$

with w_0 as the waist of the beam at position z_0, where the amplitude is $1/e$ of the initial value. The field intensity scales with $w_0/w(z)$ and with the surface area $\sim z^2$ in 3D. Lateral dispersion has to be taken into account in the

2D Gaussians, where the surface scales as $\sim z$. Hence, the factor $w_0/w(z)$ appearing as prefactor in the Gaussian pulses gets a square root in the lower dimensional case. The pulse can thus be written as

$$\vec{E}(r,z(t)) = A\,\vec{\epsilon}\sqrt{\frac{w_0}{w(z)}}\,e^{-(r/w(z))^2}\,e^{-((z-z_\tau)/\tau_z)^2}\,\cos\left(\frac{k\,r^2}{2R(z)}+\zeta(z)-kz\right)\,. \tag{87}$$

It has further been defined

- the pulse amplitude A and polarization $\vec{\epsilon}$,
- the distance to the propagation axis (here z) $r=\sqrt{x^2+y^2}$,
- the wavenumber $k=2\pi/\lambda$,
- the pulse width in z-direction τ_z and the envelope center z_τ,
- the Rayleigh length $z_R=\pi w_0^2/\lambda$ as the longitudinal distance from z_0 at which the waist has increased by a factor $\sqrt{2}$. It is contained in
  - the Gouy phase $\zeta(z)=\arctan(z/z_R)$, and
  - the beam curvature $R(z)=z(1+(z_R/z)^2)$.

The settings used for 2D simulations are listed in table 5.

Table 5: Settings for 2D simulations with two conceptually equal Gaussian pulses.
The wavelength is obtained via $\lambda=\pi w_0^2/z_R$. The Rayleigh length and waist are chosen such that the wavelength equals one micrometer.

Grid	Square Size	$80\mu m \times 80\mu m$
	Lattice Points	1024×1024
Pulse 1	$\vec{\epsilon}$	(0,0,-1)
	A	$50\mathrm{m}E_{cr}$
	$\hat{k}$	$(1,0,0)\mu m$
	λ	$1\mu m$
	w_0	$2.3\mu m$
	z_R	$16.619\mu m$
	z_τ	$20\mu m$
	τ_z	$4.5\mu m$
Pulse 2	same parameters as pulse 1, but different center position, varying propagation direction and polarization	see figure 23-32

Comparing a head-on collision in 1D (figure 21) and 2D (figure 23) a similar frequency spectrum is found at the different time states. The reasoning is the same as in section 8. The main difference stems from the fact that the two conceptionally equal pulses have the same *non-zero* frequency. There is still a degeneracy of signals present due to the equal frequencies.

As an extra feature not available in the 1D simulation a broadening of the signals in frequency space is observed – and an according sharpening of the pulse in position space which is hardly visible – in the asymptotic state. This is mostly due to 4-photon interactions as it is caused by birefringence effects that are stronger in the center of the pulses. Thus, post-collision pulses are sharper in position space and broader in the frequency domain.

Going beyond coaxial pulses by varying the collision angle and thereby lifting the degeneracy of frequencies of the harmonics, very rich spectra in 2D simulations can be observed, see figures 25-28 for perpendicularly propagating and colliding pulses as well as for an angle of 135°. Nearly all signals vanish again in the asymptotic state. In the overlap states various merging processes become directly visible, e.g. for perpendicularly colliding pulses the merging processes of 3ω and 2ω harmonics. The asymptotic states propagate only along the initial propagation axis. Videos of these simulations with $40\mu m$ propagation distance divided into 100 time steps are provided in the *Mendeley* repository [49] (thumbnail and description in figure 29).

Giving the pulses' different polarization directions, the harmonics can be tagged. The frequency space of the simulations visualized in figures 31 and 32 show again collision angles of 90°and 135°, but the pulse propagating from the right is now polarized along E_y. Hence, the shown components can be identified with one of the two pulses. Hereby the harmonic signals are tagged as they obtain the polarization of the pulse that contributes an odd number of photons.

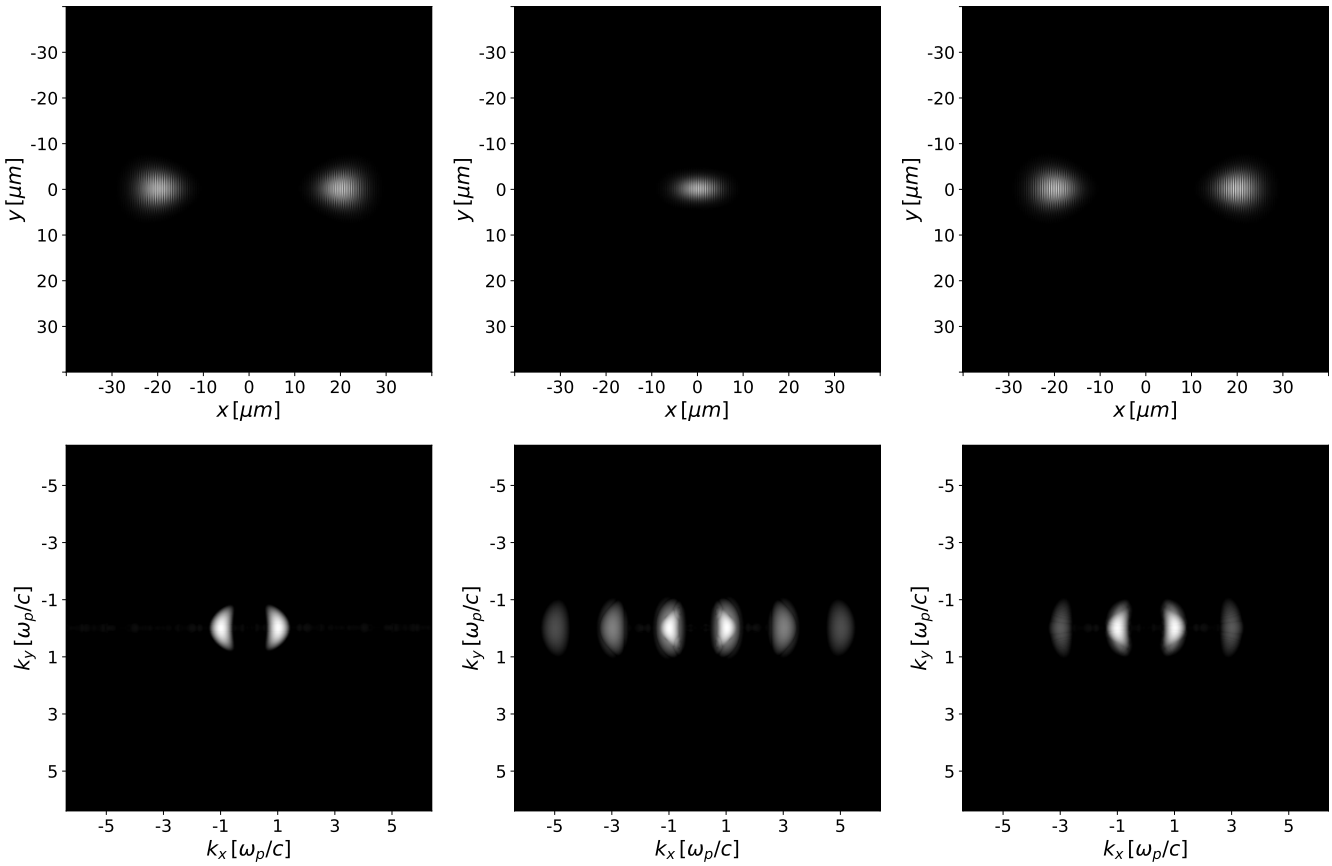

Figure 23: Coaxially colliding pulses with the same polarization. The left plots show the initial state, those in the middle the overlap state, and the right ones the final state. Top: position space. Bottom: frequency space.

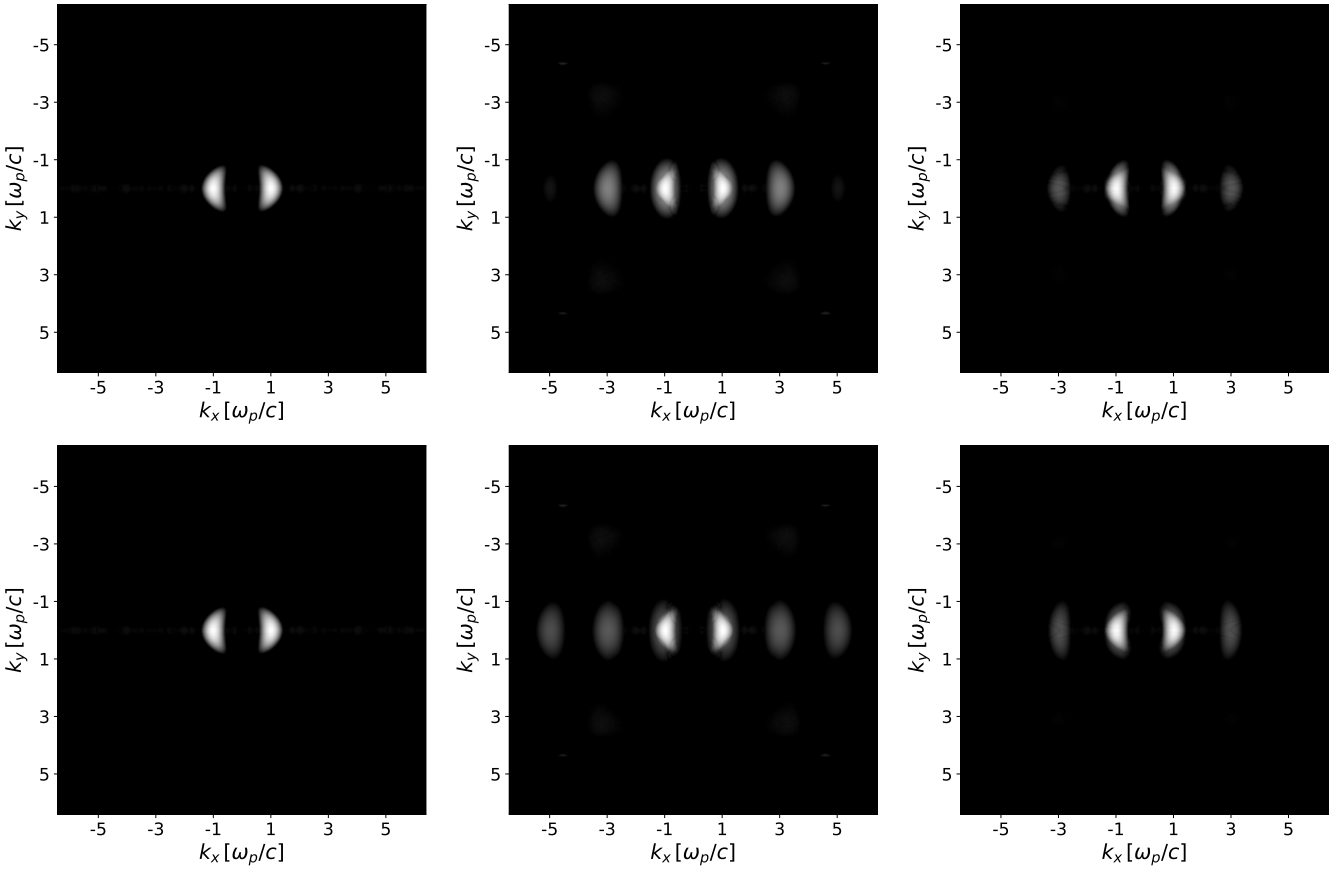

Figure 24: Frequency space of coaxially colliding pulses with the same polarization. The left plots show the initial state, those in the middle the overlap state, and the right ones the final state. Top: only 4-photon diagrams included. Bottom: only 6-photon diagrams included.

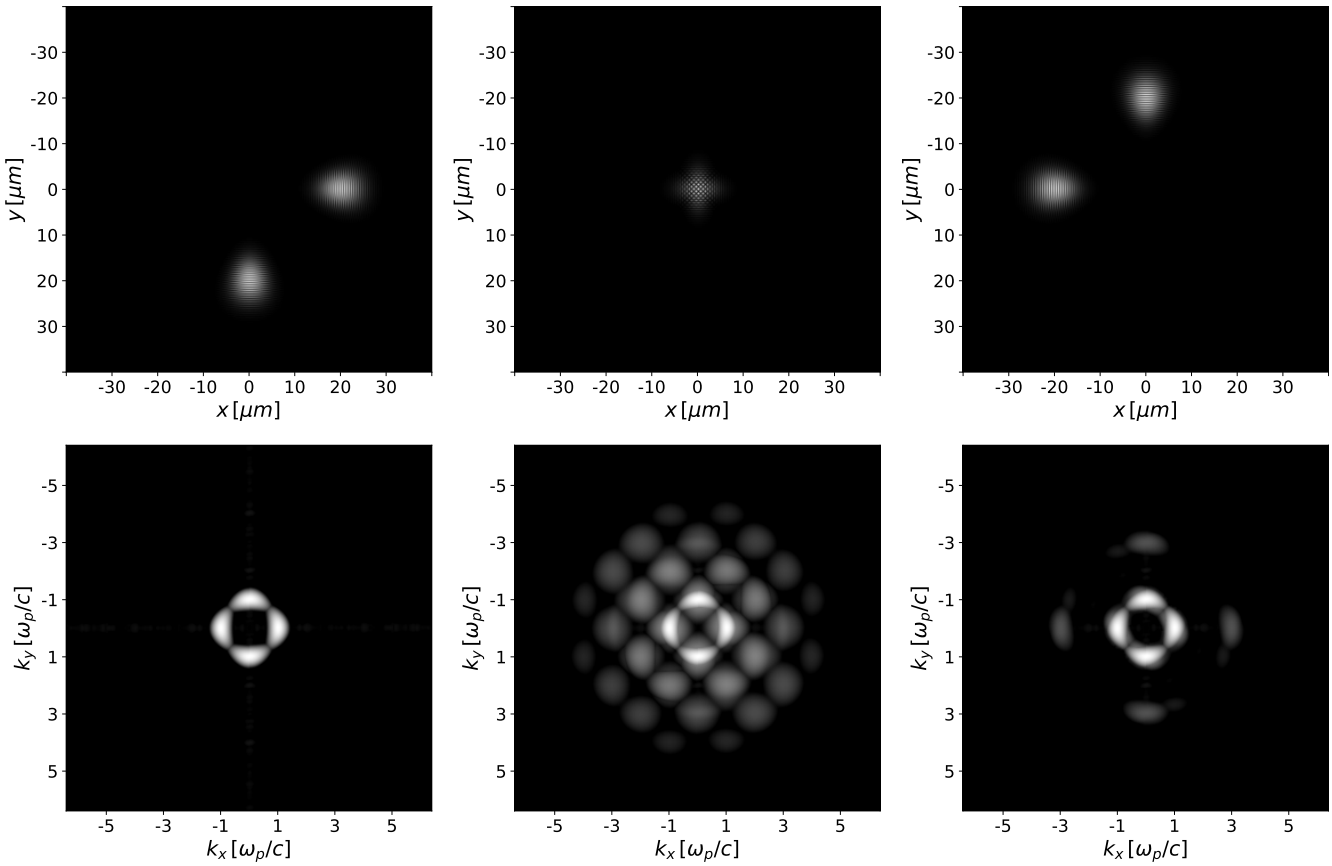

Figure 25: Perpendicularly colliding pulses with equal polarization. The left plots show the initial state, those in the middle the overlap state, and the right ones the final state. Top: position space. Bottom: frequency space.

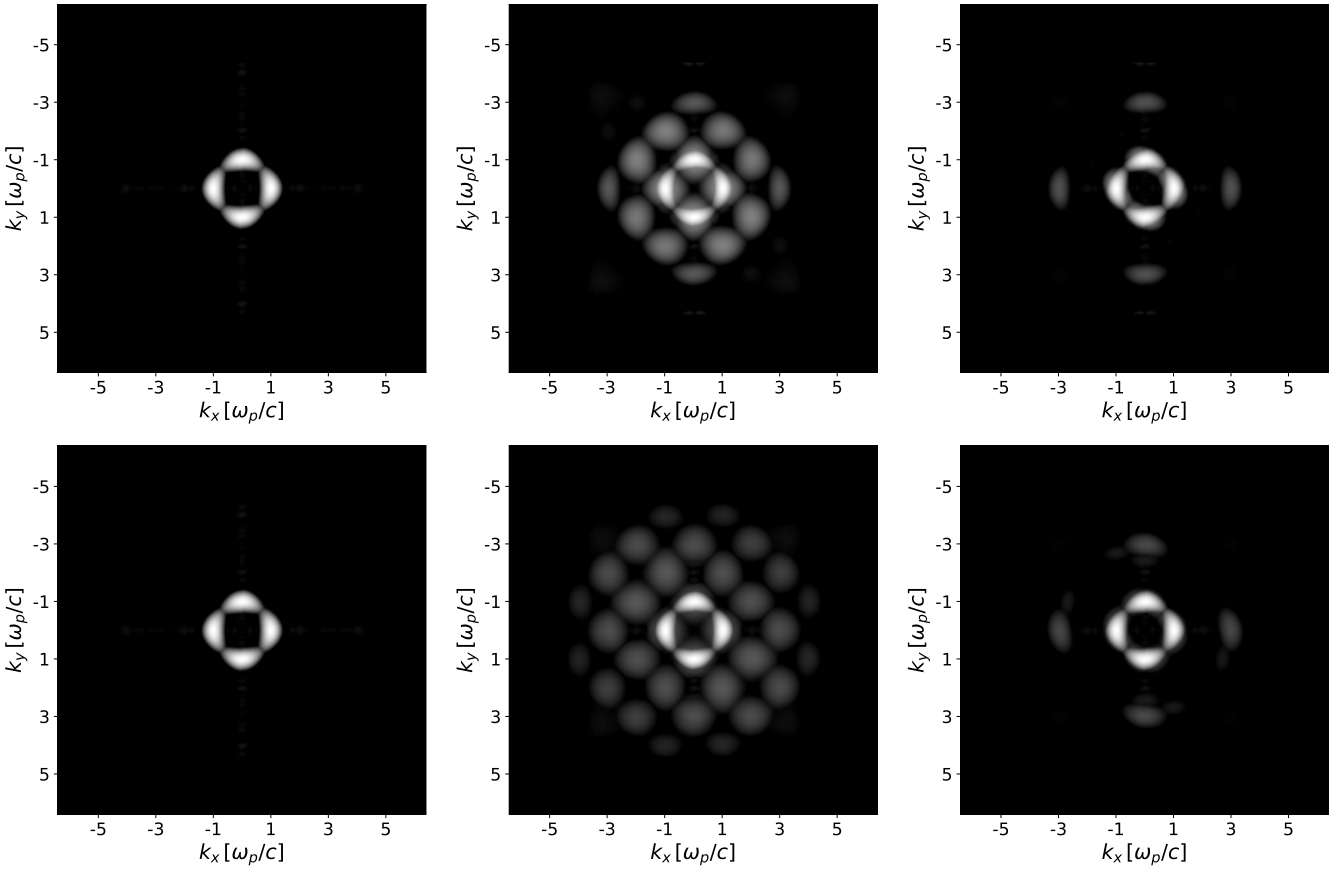

Figure 26: Frequency space of orthogonally colliding pulses with same polarization. The left plots show the initial state, those in the middle the overlap state, and the right ones the final state. Top: only 4-photon diagrams included. Bottom: only 6-photon diagrams included.

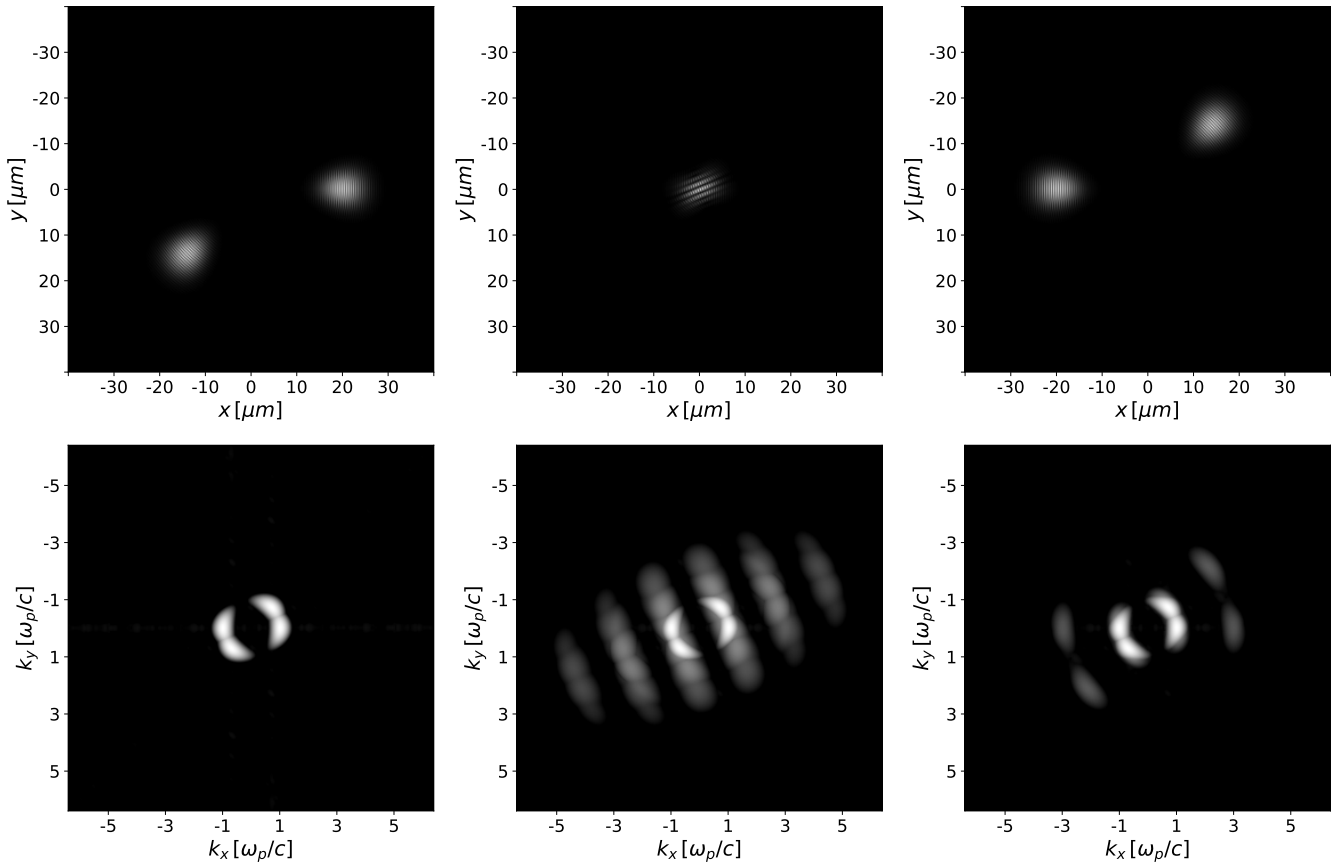

Figure 27: Pulses with the same polarization colliding at an angle of 135°. The left plots show the initial state, those in the middle the overlap state, and the right ones the final state. Top: position space. Bottom: frequency space.

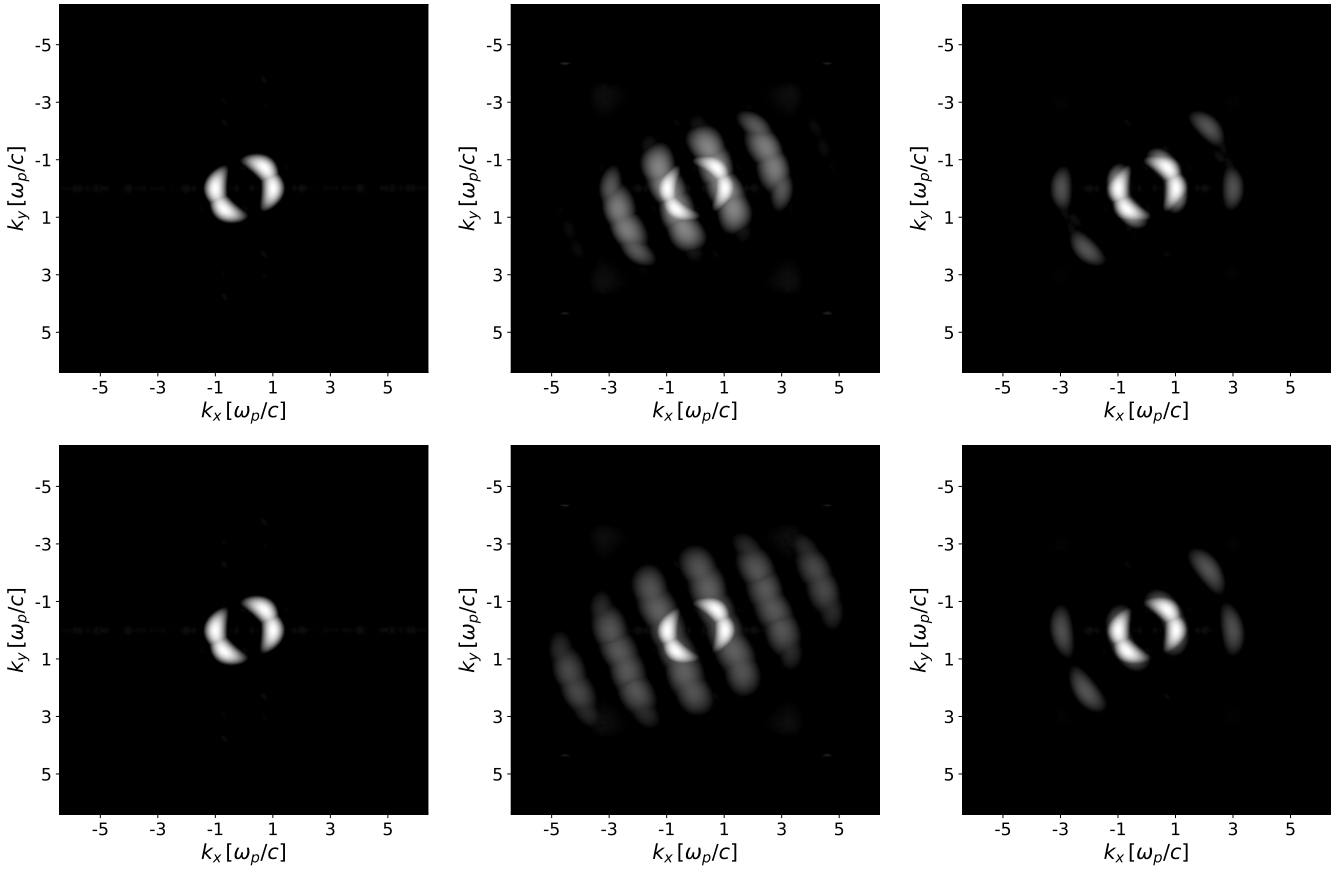

Figure 28: Frequency space of pulses with the same polarization colliding at an angle of 135°. The left plots show the initial state, those in the middle the overlap state, and the right ones the final state. Top: only 4-photon diagrams included. Bottom: only 6-photon diagrams included.

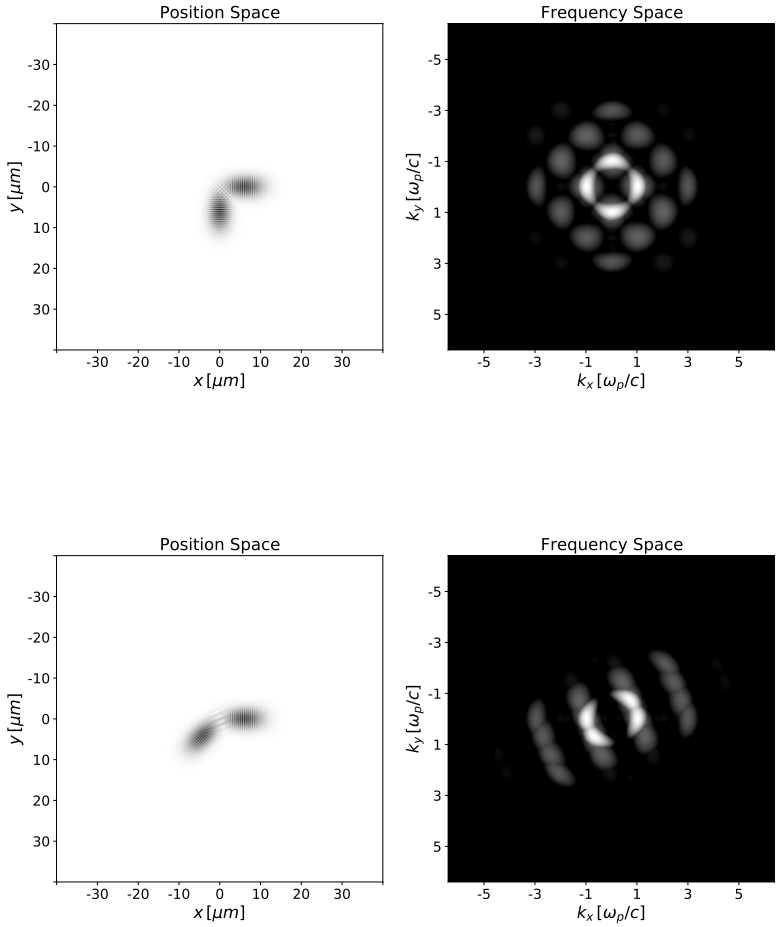

Figure 29: Thumbnail of simulation videos for two pulses colliding at an angle of 90°and 135°provided in the *Mendeley* repository [49]. Note that the 2D Gaussians extend over the whole space with foothill packets of non-zero amplitudes as sketched in figure 30 below– the graphical display in position space visualizes only the parts with amplitudes crossing a certain threshold. Therefore there are interactions already after the first time step and slightly wiggling 3ω harmonics become visible in the highly sensitive log-scale frequency space plots even before the overlap harmonics arise.

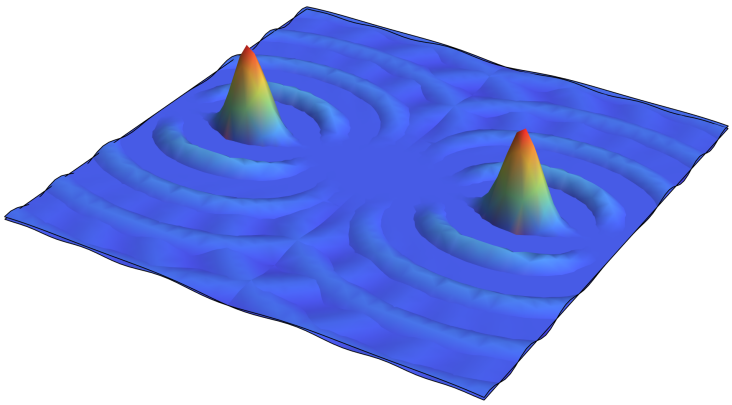

Figure 30: Schematic visualization of two Gaussians as they are implemented in the simulation space.

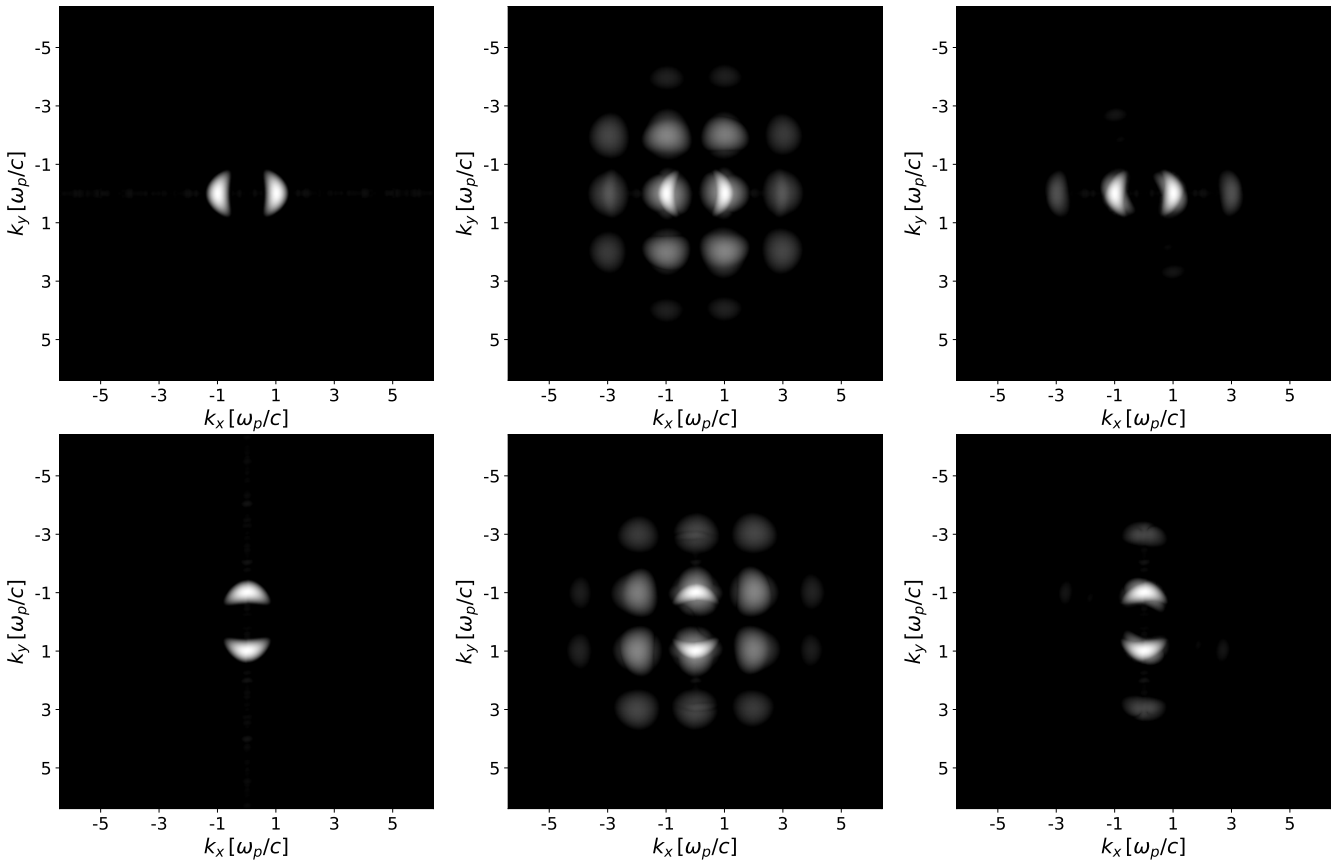

Figure 31: Frequency space of perpendicularly colliding pulses with orthogonal relative polarization. The left plots show the initial state, those in the middle the overlap state, and the right ones the final state. Top: the E_z component is shown. Bottom: the B_z component is shown.

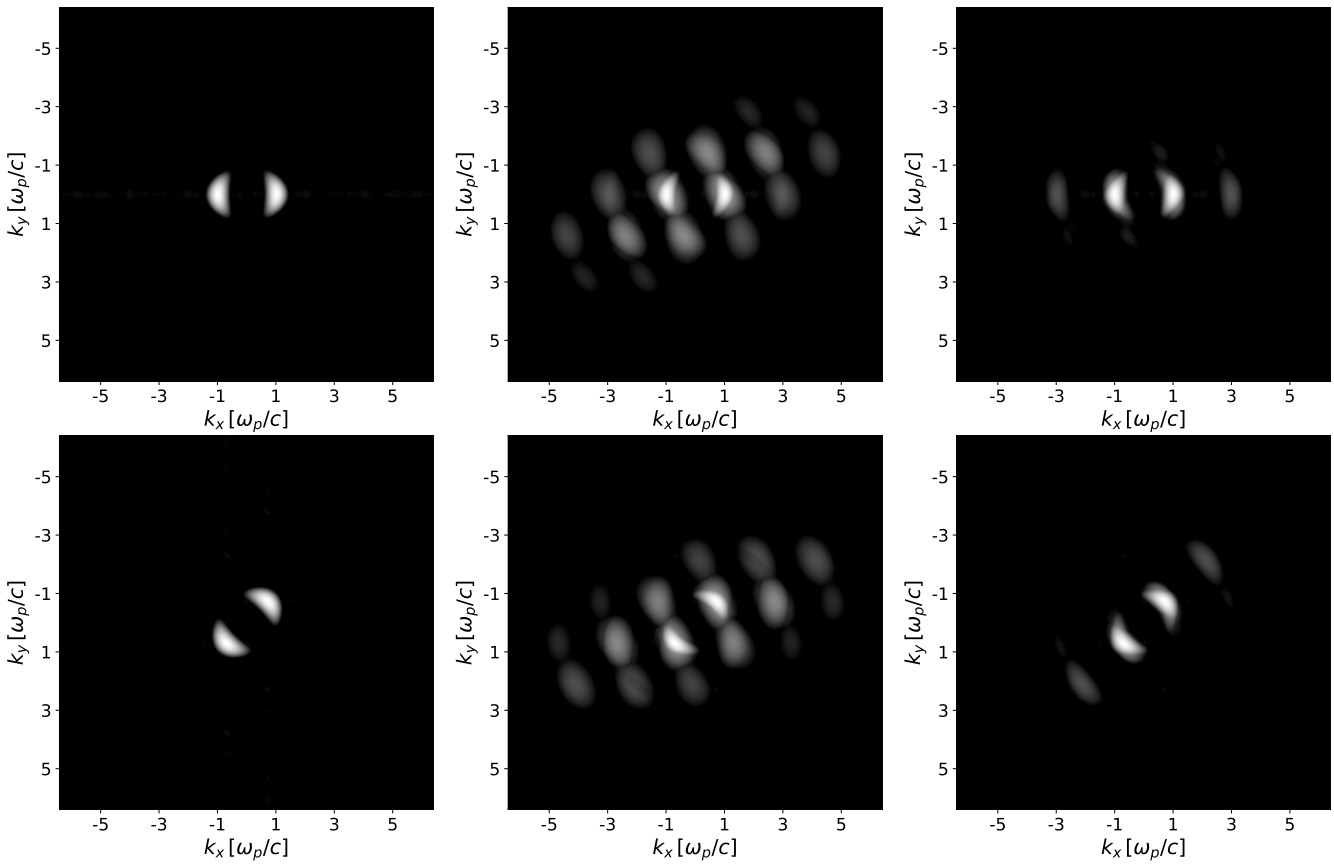

Figure 32: Frequency space of pulses colliding at an angle of 135° with orthogonal relative polarization. The left plots show the initial state, those in the middle the overlap state, and the right ones the final state. Top: the E_z component is shown. Bottom: the B_z component is shown.

10. Conclusion and Outlook

A numerical scheme solving the Heisenberg-Euler equations in three spatial dimensions in the weak-field expansion has been presented. The basic assumptions restrict to field strengths below the critical values and wavelengths larger than the Compton length of the electron.

The current C++ implementation allows simulations for up to 6-photon processes and, remarkably, distinct simulations for the linear Maxwell vacuum, only 4-photon processes, or only 6-photon processes. Every simulation includes the complete picture of the Heisenberg-Euler nonlinear physics. Analytical calculations normally concentrate on single effects alone, leaving others aside. Moreover, the agnosticism of the numerical approach to pulse configurations is its main raison d'être as a complement to theoretical treatments. Special effects of interest are extracted by a proper dedicated post-processing. The fact that not individual photon quanta but whole pulses are simulated is not hampering the analysis. On the contrary, it is striking to see such good agreement to analytical results. This is due to the high orders both in the numerical scheme and the effective expansion.

Since all simulations can be divided into an arbitrary number of time steps, the simulations permit to time-resolve any process, which is beyond the scope of many analytical approaches concentrating on asymptotic values alone.

The numerical complexity scales considerably fast with the number of lattice points, the resolution, and the dimension. It has to be stated again here that a sufficiently high grid resolution is demanded by the dispersion relation for well-behaved waves. The resolution has to be tuned in wise prospect to the signals which are attempted to be observed. Therefore, computations can become costly quite easily.

The scope of this code is far-reaching. The main purpose of the present paper is to introduce the simulation algorithm and to prove its validity. As a proven solver of the Heisenberg-Euler dynamics its usefulness in today's strong-field QED research is indisputable. Not only the high-energy, low-intensity regime employed in particle accelerators, but also the low-energy, high-intensity regime might be a path towards new physics [58]. As the quantum fluctuations in the vacuum theoretically consist of all particles there are, it may also serve as a portal to new physics [33].

As a use case it is planned to conduct a characterization of strong pulses by propagating probe pulses through them and analyzing the asymptotic states of the latter. These reveal information about the pump frequency via harmonic generation on the one hand and about the polarization and field strength via polarization flipping of the probe on the other hand, as has been shown in the present work. This non-invasive approach is to ultimately subside detector material where intensities become too high. There has been theoretical work on such scattering configurations that may serve as a benchmark [34].

The code is capable of multi-scale simulations. In ongoing studies the behavior of simulated waves at a grid resolution barrier is investigated. This research is intended to pave the way for a dynamical grid adapting its resolution regionally on the fly and on demand in order to reduce the computational load while at the same time maximizing the accuracy in important spatial regions. Simulating the whole space from the initial to final states of all participating pulses in a grid of uniform high resolution – which has to be suited for the highest-frequency pulse – is very expensive. An adaptive grid is especially suited for the prominent low-frequency pump and high-frequency probe pulses setup to detect vacuum nonlinearities where the computational load can in principle be dramatically reduced.

Furthermore, it is the authors' aim to provide colleagues in the research group who study optical signatures of vacuum effects in high intensity fields with numerical results. To this end it will be attempted to reproduce the settings and findings of [33, 35–37]. The goal is to provide an indispensable tool for experimentalists to second their setups with simulation data.

In a follow-up work a first phenomenological analysis in 3D has to be performed. Besides the scaling test no results are shown of 3D simulations in this paper due to the heavy numerical load required to produce sensible data. A current task is thus the improvement of large scalability as mentioned in section 5. It is a huge step forward to finally go beyond lower dimensional approximations on the numerical side.

Acknowledgments

This work has been funded by the Deutsche Forschungsgemeinschaft (DFG) under Grant No. 416699545 within the Research Unit FOR 2783/1.

The authors want to thank all the members and friends of FOR 2783 for their support and the fruitful discussions during the research group retreats and beyond. Special thanks are due to Holger Gies, Carsten Müller, and Alina Golub.

In the first place, however, the fantastic preliminary work of Arnau Pons Domenech has to be emphasized. Together with Hartmut Ruhl, he initially devised the numerical algorithm and developed the code. This paper is based on his PhD project.

The computations have been performed on the KSC cluster computing system of the Arnold Sommerfeld Center for theoretical physics at LMU Munich, hosted at the Leibniz-Rechenzentrum (LRZ) in Garching and funded by the German Research Foundation (DFG) under the project number 409562408.

Data Statement

The raw simulation data used for this work amount to 20GB in size. It is archived on servers of the Arnold Sommerfeld Cluster (ASC) hosted by the Leibniz-Rechenzentrum (LRZ) in compliance with the regulatories of the German Research Foundation (DFG). The code is maintained on an institutional GitLab server and will be made publicly available.

References

[1] W. Heisenberg, H. Euler, Folgerungen aus der Diracschen Theorie des Positrons, Zeitschrift für Physik 98 (11) (1935) 714–732. doi:10.1007/BF01343663.
URL http://dx.doi.org/10.1007/BF01343663

[2] J. Schwinger, On Gauge Invariance and Vacuum Polarization, Phys. Rev. 82 (1951) 664–679. doi:10.1103/PhysRev.82.664.
URL http://link.aps.org/doi/10.1103/PhysRev.82.664

[3] J. Toll, The dispersion relation for light and its application to problems involving electron pairs, Ph.D. thesis, Princeton University, (unpublished) (1952).

[4] R. Baier, P. Breitenlohner, The vacuum refraction index in the presence of external fields, Il Nuovo Cimento B Series 10 47 (1) (1967) 117–120. doi:10.1007/BF02712312.
URL http://dx.doi.org/10.1007/BF02712312

[5] T. Heinzl, B. Liesfeld, K.-U. Amthor, H. Schwoerer, R. Sauerbrey, A. Wipf, On the observation of vacuum birefringence, Optics Communications 267 (2) (2006) 318 – 321. doi:http://dx.doi.org/10.1016/j.optcom.2006.06.053.
URL http://www.sciencedirect.com/science/article/pii/S0030401806006481

[6] B. J. King, Vacuum polarisation effects in intense laser fields, Ph.D. thesis, Ruprecht-Karls-Universität Heidelberg (2010).
URL https://archiv.ub.uni-heidelberg.de/volltextserver/10846/

[7] D. Tommasini, H. Michinel, Light by light diffraction in vacuum, Phys. Rev. A 82 (2010) 011803. doi:10.1103/PhysRevA.82.011803.
URL http://link.aps.org/doi/10.1103/PhysRevA.82.011803

[8] Y. Monden, R. Kodama, Enhancement of Laser Interaction with Vacuum for a Large Angular Aperture, Phys. Rev. Lett. 107 (2011) 073602. doi:10.1103/PhysRevLett.107.073602.
URL http://link.aps.org/doi/10.1103/PhysRevLett.107.073602

[9] A. Di Piazza, K. Z. Hatsagortsyan, C. H. Keitel, Light Diffraction by a Strong Standing Electromagnetic Wave, Phys. Rev. Lett. 97 (2006) 083603. doi:10.1103/PhysRevLett.97.083603.
URL https://link.aps.org/doi/10.1103/PhysRevLett.97.083603

[10] B. King, A. Di Piazza, C. H. Keitel, A matterless double slit, Nature Photonics 4 (2) (2010) 92–94.
URL https://www.nature.com/articles/nphoton.2009.261#citeas

[11] S. L. Adler, Photon splitting and photon dispersion in a strong magnetic field, Annals of Physics 67 (2) (1971) 599 – 647. doi:http://dx.doi.org/10.1016/0003-4916(71)90154-0.
URL http://www.sciencedirect.com/science/article/pii/0003491671901540

[12] B. King, C. H. Keitel, Photon–photon scattering in collisions of intense laser pulses, New Journal of Physics 14 (10) (2012) 103002.
URL http://stacks.iop.org/1367-2630/14/i=10/a=103002

[13] H. Gies, F. Karbstein, N. Seegert, Quantum reflection as a new signature of quantum vacuum nonlinearity, New Journal of Physics 15 (8) (2013) 083002.
URL http://stacks.iop.org/1367-2630/15/i=8/a=083002

[14] P. Böhl, B. King, H. Ruhl, Vacuum high-harmonic generation in the shock regime, Phys. Rev. A 92 (2015) 032115. doi:10.1103/PhysRevA.92.032115.
URL http://link.aps.org/doi/10.1103/PhysRevA.92.032115

[15] P. A. Böhl, Vacuum harmonic generation in slowly varying electromagnetic backgrounds, Ph.D. thesis, lmu (2016).
URL https://edoc.ub.uni-muenchen.de/19887

[16] A. Fedotov, N. Narozhny, Generation of harmonics by a focused laser beam in the vacuum, Physics Letters A 362 (1) (2007) 1–5.
URL https://doi.org/10.1016/j.physleta.2006.09.085

[17] B. King, P. Böhl, H. Ruhl, Interaction of photons traversing a slowly varying electromagnetic background, Phys. Rev. D 90 (2014) 065018. doi:10.1103/PhysRevD.90.065018.
URL http://link.aps.org/doi/10.1103/PhysRevD.90.065018

[18] Z. Bialynicka-Birula, I. Bialynicki-Birula, Nonlinear Effects in Quantum Electrodynamics. Photon Propagation and Photon Splitting in an External Field, Phys. Rev. D 2 (1970) 2341–2345. doi:10.1103/PhysRevD.2.2341.
URL https://link.aps.org/doi/10.1103/PhysRevD.2.2341

[19] A. Di Piazza, A. I. Milstein, C. H. Keitel, Photon splitting in a laser field, Phys. Rev. A 76 (2007) 032103. doi:10.1103/PhysRevA.76.032103.
URL https://link.aps.org/doi/10.1103/PhysRevA.76.032103

[20] C. N. Danson, C. Haefner, J. Bromage, T. Butcher, J.-C. F. Chanteloup, E. A. Chowdhury, A. Galvanauskas, L. A. Gizzi, J. Hein, D. I. Hillier, et al., Petawatt and exawatt class lasers worldwide, High Power Laser Science and Engineering 7 (2019) e54. doi:10.1017/hpl.2019.36.
URL https://doi.org/10.1017/hpl.2019.36

[21] M. Scholz, FEL Performance Achieved at European XFEL, in: Proc. 9th International Particle Accelerator Conference (IPAC'18), Vancouver, BC, Canada, April 29-May 4, 2018, no. 9 in International Particle Accelerator Conference, JACoW Publishing, Geneva, Switzerland, 2018, pp. 29–33, https://doi.org/10.18429/JACoW-IPAC2018-MOZGBD2. doi:doi:10.18429/JACoW-IPAC2018-MOZGBD2.
URL http://jacow.org/ipac2018/papers/mozgbd2.pdf

[22] E. Lundstrom, G. Brodin, J. Lundin, M. Marklund, R. Bingham, J. Collier, J. T. Mendonca, P. Norreys, Using high-power lasers for detection of elastic photon-photon scattering, Phys. Rev. Lett. 96 (2006) 083602. arXiv:hep-ph/0510076, doi:10.1103/PhysRevLett.96.083602.

[23] J. Lundin, M. Marklund, E. Lundstrom, G. Brodin, J. Collier, R. Bingham, J. T. Mendonca, P. Norreys, Detection of elastic photon-photon scattering through four-wave mixing using high power lasers, Phys. Rev. A 74 (2006) 043821. arXiv:hep-ph/0606136, doi:10.1103/PhysRevA.74.043821.

[24] D. Tommasini, A. Ferrando, H. Michinel, M. Seco, Precision tests of QED and non-standard models by searching photon-photon scattering in vacuum with high power lasers, JHEP 11 (2009) 043. arXiv:0909.4663, doi:10.1088/1126-6708/2009/11/043.

[25] B. King, T. Heinzl, Measuring Vacuum Polarisation with High Power Lasers, arXiv preprint arXiv:1510.08456 (2015).

[26] A. N. Luiten, J. C. Petersen, Detection of vacuum birefringence using intense laser pulses, Physics Letters A 330 (6) (2004) 429 – 434. doi:http://dx.doi.org/10.1016/j.physleta.2004.08.020.
URL http://www.sciencedirect.com/science/article/pii/S0375960104011442

[27] F. Karbstein, H. Gies, M. Reuter, M. Zepf, Vacuum birefringence in strong inhomogeneous electromagnetic fields, Phys. Rev. D 92 (2015) 071301. doi:10.1103/PhysRevD.92.071301.
URL http://link.aps.org/doi/10.1103/PhysRevD.92.071301

[28] V. Dinu, T. Heinzl, A. Ilderton, M. Marklund, G. Torgrimsson, Vacuum refractive indices and helicity flip in strong-field QED, Phys. Rev. D 89 (2014) 125003. doi:10.1103/PhysRevD.89.125003.
URL http://link.aps.org/doi/10.1103/PhysRevD.89.125003

[29] V. Dinu, T. Heinzl, A. Ilderton, M. Marklund, G. Torgrimsson, Photon polarization in light-by-light scattering: Finite size effects, Phys. Rev. D 90 (2014) 045025. doi:10.1103/PhysRevD.90.045025.
URL http://link.aps.org/doi/10.1103/PhysRevD.90.045025

[30] H. Gies, F. Karbstein, C. Kohlfürst, N. Seegert, Photon-photon scattering at the high-intensity frontier, Phys. Rev. D 97 (7) (2018) 076002. arXiv:1712.06450, doi:10.1103/PhysRevD.97.076002.

[31] H. Gies, F. Karbstein, C. Kohlfürst, All-optical signatures of Strong-Field QED in the vacuum emission picture, Phys. Rev. D 97 (3) (2018) 036022. arXiv:1712.03232, doi:10.1103/PhysRevD.97.036022.

[32] B. King, H. Hu, B. Shen, Three-pulse photon-photon scattering, Phys. Rev. A 98 (2) (2018) 023817. arXiv:1805.03688, doi:10.1103/PhysRevA.98.023817.

[33] F. Karbstein, A. Blinne, H. Gies, M. Zepf, Boosting Quantum Vacuum Signatures by Coherent Harmonic Focusing, Phys. Rev. Lett. 123 (2019) 091802. doi:10.1103/PhysRevLett.123.091802.
URL https://link.aps.org/doi/10.1103/PhysRevLett.123.091802

[34] F. Karbstein, E. A. Mosman, X-ray photon scattering at a focused high-intensity laser pulse, Phys. Rev. D 100 (2019) 033002. doi:10.1103/PhysRevD.100.033002.
URL https://link.aps.org/doi/10.1103/PhysRevD.100.033002

[35] F. Karbstein, Probing Vacuum Polarization Effects with High-Intensity Lasers, Particles 3 (1) (2020) 39–61. doi:10.3390/particles3010005.
URL https://www.mdpi.com/2571-712X/3/1/5

[36] F. Karbstein, E. A. Mosman, Enhancing quantum vacuum signatures with tailored laser beams, Phys. Rev. D 101 (2020) 113002. doi:10.1103/PhysRevD.101.113002.
URL https://link.aps.org/doi/10.1103/PhysRevD.101.113002

[37] L. Klar, Detectable Optical Signatures of QED Vacuum Nonlinearities Using High-Intensity Laser Fields, Particles 3 (1) (2020) 223–233. doi:10.3390/particles3010018.
URL https://www.mdpi.com/2571-712X/3/1/18

[38] A. P. Domenech, H. Ruhl, An implicit ODE-based numerical solver for the simulation of the Heisenberg-Euler equations in 3+1 dimensions (2017). arXiv:1607.00253.

[39] A. Pons Domenech, Simulation of quantum vacuum in higher dimensions, Ph.D. thesis, lmu (2018).
URL https://edoc.ub.uni-muenchen.de/21885/

[40] A. Blinne, H. Gies, F. Karbstein, C. Kohlfürst, M. Zepf, All-optical signatures of quantum vacuum nonlinearities in generic laser fields, Phys. Rev. D 99 (2019) 016006. doi:10.1103/PhysRevD.99.016006.
URL https://link.aps.org/doi/10.1103/PhysRevD.99.016006

[41] F. Karbstein, R. Shaisultanov, Stimulated photon emission from the vacuum, Phys. Rev. D 91 (2015) 113002. doi:10.1103/PhysRevD.91.113002.
URL https://link.aps.org/doi/10.1103/PhysRevD.91.113002

[42] A. Blinne, S. Kuschel, S. Tietze, M. Zepf, Efficient retrieval of phase information from real-valued electromagnetic field data, Journal of Computational Physics: X 1 (2019) 100019. doi:https://doi.org/10.1016/j.jcpx.2019.100019.
URL https://www.sciencedirect.com/science/article/pii/S2590055219300356

[43] T. Grismayer, R. Torres, P. Carneiro, F. Cruz, R. A. Fonseca, L. O. Silva, Quantum electrodynamics vacuum polarization solver, New Journal of Physics 23 (9) (2021) 095005. doi:10.1088/1367-2630/ac2004.
URL https://doi.org/10.1088/1367-2630/ac2004

[44] G. V. Dunne, T. M. Hall, Borel summation of the derivative expansion and effective actions, Phys. Rev. D 60 (1999) 065002. doi:10.1103/PhysRevD.60.065002.
URL http://link.aps.org/doi/10.1103/PhysRevD.60.065002

[45] H. Gies, L. Roessler, Vacuum polarization tensor in inhomogeneous magnetic fields, Phys. Rev. D 84 (2011) 065035. doi:10.1103/PhysRevD.84.065035.
URL http://link.aps.org/doi/10.1103/PhysRevD.84.065035

[46] E. Tiesinga, P. J. Mohr, D. B. Newell, B. N. Taylor, Codata recommended values of the fundamental physical constants: 2018, Rev. Mod. Phys. 93 (2021) 025010. doi:10.1103/RevModPhys.93.025010.
URL https://link.aps.org/doi/10.1103/RevModPhys.93.025010

[47] J. C. Maxwell, A Dynamical Theory of the Electromagnetic Field, Philosophical Transactions of the Royal Society of London 155 (1865) 459–512. doi:10.1098/rstl.1865.0008.
URL http://rstl.royalsocietypublishing.org/content/155/459.short

[48] W. H. Press, S. A. Teukolsky, W. T. Vetterling, B. P. Flannery, Numerical Recipes 3rd Edition: The Art of Scientific Computing, 3rd Edition, Cambridge University Press, 2007.

[49] A. Lindner, HEWES project extra and supportive material, Mendeley Data (2022). doi:10.17632/f9wntyw39x.1.

[50] E. Hairer, S. P. Nørsett, G. Wanner, Solving ordinary differential equations. I, Nonstiff problems, Springer-Vlg, 1993.

[51] A. C. Hindmarsh, P. N. Brown, K. E. Grant, S. L. Lee, R. Serban, D. E. Shumaker, C. S. Woodward, SUNDIALS: Suite of nonlinear and differential/algebraic equation solvers, ACM Transactions on Mathematical Software (TOMS) 31 (3) (2005) 363–396.

[52] P. Virtanen, R. Gommers, T. E. Oliphant, M. Haberland, T. Reddy, D. Cournapeau, E. Burovski, P. Peterson, W. Weckesser, J. Bright, S. J. van der Walt, M. Brett, J. Wilson, K. J. Millman, N. Mayorov, A. R. J. Nelson, E. Jones, R. Kern, E. Larson, C. J. Carey, İ. Polat, Y. Feng, E. W. Moore, J. VanderPlas, D. Laxalde, J. Perktold, R. Cimrman, I. Henriksen, E. A. Quintero, C. R. Harris, A. M. Archibald, A. H. Ribeiro, F. Pedregosa, P. van Mulbregt, SciPy 1.0 Contributors, SciPy 1.0: Fundamental Algorithms for Scientific Computing in Python, Nature Methods 17 (2020) 261–272. doi:10.1038/s41592-019-0686-2.

[53] T. Kluyver, B. Ragan-Kelley, F. Pérez, B. Granger, M. Bussonnier, J. Frederic, K. Kelley, J. Hamrick, J. Grout, S. Corlay, P. Ivanov, D. Avila, S. Abdalla, C. Willing, Jupyter notebooks – a publishing format for reproducible computational workflows, in: F. Loizides, B. Schmidt (Eds.), Positioning and Power in Academic Publishing: Players, Agents and Agendas, IOS Press, 2016, pp. 87 – 90.

[54] W. R. Inc., Mathematica, Version 12.3, champaign, IL (2021).
URL https://www.wolfram.com/mathematica

[55] L. Clarke, I. Glendinning, R. Hempel, The MPI message passing interface standard, in: Programming environments for massively parallel distributed systems, Springer, 1994, pp. 213–218.

[56] Intel® Corporation, Intel® oneapi™programming guide (2022).
URL https://www.intel.com/content/www/us/en/develop/documentation/oneapi-programming-guide/

[57] W. Dittrich, H. Gies, Probing the Quantum Vacuum: Perturbative Effective Action Approach in Quantum Electrodynamics and its Application, Springer Tracts in Modern Physics, Springer Berlin Heidelberg, 2003.
URL https://books.google.de/books?id=lctrCQAAQBAJ

[58] H. Gies, Strong laser fields as a probe for fundamental physics, Eur. Phys. J. D 55 (2009) 311–317. arXiv:0812.0668, doi:10.1140/epjd/e2009-00006-0.